SIAM J. APPLIED DYNAMICAL SYSTEMS
Vol. 21, No. 3, pp. 1952–1999

© 2022 Society for Industrial and Applied Mathematics

Downloaded 09/04/22 to 130.49.198.139 . Redistribution subject to SIAM license or copyright; see https://epubs.siam.org/terms-privacy

Activity Patterns of a Two-Timescale Neuronal Ring Model with Voltage-Dependent, Piecewise Smooth Inhibitory Coupling[*]

Choongseok Park[†] and Jonathan E. Rubin[‡]

Abstract. We present an analysis of activity patterns in a neuronal network that consists of three mutually inhibitory neurons with voltage-sensitive piecewise smooth coupling. This network model is motivated by the respiratory neuronal network in the mammalian brainstem and is able to exhibit various activity patterns including bistability of relaxation oscillation solutions in which activation propagates around the ring in opposite directions. One of the observed propagating solutions appears to be contrary to the network architecture and is characterized by a sudden "turn-around" of trajectories during fast transitions between quasi-stable states. Standard fast-slow analysis provides the set of fast subsystem fixed points and transition surfaces parametrized by slow variables, but due to the voltage-sensitive nature of the coupling it fails to describe the mechanism underlying the sudden "turn-around" during fast jumps. By considering a linear, reduced form of the model system that preserves the solution structure, we are able to perform a thorough analysis of the oscillations, which reveals novel *adaptive escape* and *adaptive release* phase transition mechanisms. To determine where the fast jumps actually go, we exploit the piecewise smooth nature of the coupling to consider a sequence of fast subsystems defined in a piecewise way. Our analysis shows that there are three possible scenarios during fast jumps, which may depend on both the fast dynamics and the slow dynamics. First, the fast dynamics may succeed to equilibrate at (or near) a critical manifold branch, after which the slow dynamics relaxes to its own fixed point, pulling the slaved fast variables along the critical manifold. Second, while the fast dynamics tries to equilibrate to a critical manifold, the slow dynamics may push the fast system through a bifurcation, which forces a second fast jump to a new critical manifold component, after which the slow relaxation follows. Third, the critical manifold component expected to be attracting may be lost prior to fast subsystem equilibration or may be inaccessible due to separatrix geometry, in which case the fast dynamics is forced to approach a new critical manifold directly. In the second and third cases, we observe the sudden"turn-around" during fast jumps.

Key words. relaxation oscillations, synaptic coupling, neuronal dynamics, fast-slow decomposition, bifurcation

MSC codes. 34A12, 34A34, 34C15, 34C60, 37G15, 37N25, 92B20, 92B25

DOI. 10.1137/21M1431679

1. Introduction.

Rhythmic activity patterns arise in various regions of the central nervous system and have been implicated in a variety of critical and cognitive functions [52, 13, 6]. Some well-known examples of the former include neural signaling, generated by circuits known as central pattern generators (CPGs), which underlies stereotyped, rhythmic behaviors such

---

[*] Received by the editors July 6, 2021; accepted for publication (in revised form) April 10, 2022; published electronically July 28, 2022.
https://doi.org/10.1137/21M1431679
Funding: The work of the first author was partially supported by NSF HRD-1700199. The work of the second author was partially supported by NSF award DMS-1951095.

[†] Department of Mathematics, North Carolina A&T State University, Greensboro, NC 27411 USA (cpark@ncat.edu).

[‡] Department of Mathematics, University of Pittsburgh, Pittsburgh, PA 15260 USA (jonrubin@pitt.edu).

Copyright © by SIAM. Unauthorized reproduction of this article is prohibited.

Downloaded 09/04/22 to 130.49.198.139 . Redistribution subject to SIAM license or copyright; see https://epubs.siam.org/terms-privacy

as respiration, digestion, and some forms of feeding and locomotion [20, 26, 25]. While there is clear evidence that CPGs drive many such behaviors across a wide range of species, it is unlikely that there is a one-to-one mapping between specialized CPG circuits and repetitive behaviors. The concept of a multifunctional neuron pool has been introduced to describe a neuronal circuit that, depending on the tonic or transient inputs that it receives and its initial conditions, can produce more than one stable output pattern [5]. For example, on the simpler end of the behavioral continuum, there is clear evidence that the same core respiratory CPG can reconfigure its activity to produce multiple forms of respiratory output including forced expiration and gasping, while in more complicated motor behaviors, the same neural circuit may produce multiple different gait patterns [19] or even different forms of motor output such as swimming and scratching [2, 21] or swimming and crawling [5].

To understand how CPGs and other rhythmic neural networks maintain functionality across physiologic states and environmental and behavioral demands and potentially reconfigure to produce different outputs, it is crucial to study the mechanisms underlying rhythm generation and regulation within these circuits. Networks involving mutual inhibition among individual neurons or neuronal populations comprise key components within a variety of CPGs [33, 16, 15, 24] and have been extensively studied from experimental and computational perspectives due to the importance that they hold for biological function, the accessibility that they afford for experimentalists, and the interesting dynamics that they exhibit. Previous computational analysis of these circuits has proceeded along several lines of investigation. Various works have combined numerical simulations and analytical study, often involving bifurcation analysis, to characterize how tuning of parameters including tonic input levels affects the properties of specific rhythmic patterns, as well as deletions of certain phases within these patterns [41, 35, 27, 51, 7]. Some past work has focused on how changes in synaptic coupling strengths in a circuit with a fixed network architecture can result in specific output pattern switches, such as the transition between swimming and scratching patterns [21, 45, 4, 31, 32]. On the methodological side, an analytical technique has been derived to compute a mapping between regions in phase space and repeated activation patterns in mutually inhibitory circuits composed of planar neuronal models with fast-slow dynamics and has been illustrated in a three-component representation of the respiratory CPG [39]. Indeed, many of these works have exploited the multiple timescale structure of neuronal models, in which voltage and some ion channel gating variables evolve at a much faster rate than other system components such as some additional gating variables and ion concentrations, to conduct analysis based on a fast-slow decomposition [34, 38, 3].

In the present computational and analytical study, we adopt a somewhat different perspective from these earlier analyses. We consider a simplified, three-component neuronal circuit with all-to-all inhibitory coupling. As in some past works, we break the symmetry in the synaptic weights in a way that would be expected to produce a bias in the activation order of the units in the circuit [18]. In this setting, we examine an unexpected variety in solution features that emerges as the connection strengths within the network are varied together, including a bistability of patterns with different activation orders that arise and maintain stability over a surprisingly wide, overlapping range of parameter values. Although our model neurons are typical fast-slow units, our analysis highlights some unexpected subtlety in the interaction of the fast and slow dynamics. Our results could be interpreted as a

Copyright © by SIAM. Unauthorized reproduction of this article is prohibited.

Downloaded 09/04/22 to 130.49.198.139 . Redistribution subject to SIAM license or copyright; see https://epubs.siam.org/terms-privacy

warning against the use of simple three-unit inhibitory CPG models, with symmetry breaking in synaptic weights used to impose directionality, to represent circuits known to produce a specific activity pattern. On the other hand, our results could also be interpreted as evidence in favor of the concept that a single neuronal circuit with reciprocal inhibition can serve as a multifunctional neuron pool that produces multiple output patterns (see [5, 21, 31] and the references therein) selected by a choice of initial activation signals.

The remainder of this paper is organized as follows. In section 2, we present the main model that represents the starting point of this work, we illustrate the types of solutions that we study, and we present associated bifurcation diagrams. In section 3, we analyze key aspects of the dynamics in a pair of simplified linear models: first a two-cell network and next a three-cell network. This analysis includes a variety of steps that lead to an understanding of the interaction of fast and slow dynamic mechanisms that shape the model solutions that emerge. After presenting this analysis, we consider how the insights that are derived apply to the original model. Finally, in section 4, we conclude with a discussion that highlights six lessons that are revealed by the analysis that we have performed.

2. Neuronal network model and dynamics.

2.1. Model formulation.

We consider the activity patterns of a neuronal network composed of three units each coupled to the other two by synaptic inhibition. All units are represented with a nonspiking model, variations of which have been adopted in past works for several reasons: as analytically tractable models of neuronal dynamics (e.g., [30, 46, 43, 47, 22, 39]), to represent CPG neurons that generate up and down states but do not actually spike [10], and as a simplified representation of populations of neurons that switch synchronously between silent quiescent phases and active spiking phases but with asynchronous spike generation within the active phase [35, 28, 1, 37]. Although these multiple interpretations are possible, we henceforth refer to each unit in the network as a neuron. For concreteness, we use a model introduced in studying the generation of respiratory rhythms in the brainstem [35]; under baseline conditions, respiration is a three-phase rhythm that is viewed as involving a mutually inhibitory three-unit circuit [33, 40, 44, 29].

The dynamics of each neuron is described by two differential equations, one for voltage (v_i) and the other for adaptation (m_i), for $i \in \{1, 2, 3\}$:

$$\begin{aligned} \dot{v}_i &= (-I_{\mathrm{AD}i} - I_{\mathrm{L}i} - I_{\mathrm{SynI}i} - I_{\mathrm{SynE}i})/C, \\ \dot{m}_i &= (-m_i + K_{\mathrm{AD}} f(v_i))/\tau_{\mathrm{AD}}, \end{aligned} \tag{2.1}$$

where the adaptation current $I_{\mathrm{AD}i} = g_{\mathrm{AD}} m_i (v_i - v_{\mathrm{K}})$, with maximal conductance g_{AD} and reversal potential v_{K}, and the leak current $I_{\mathrm{L}i} = g_{\mathrm{L}}(v_i - v_{\mathrm{L}})$, with conductance g_{L} and reversal potential v_{L}. Inhibitory and excitatory synaptic currents are given by

$$\begin{aligned} I_{\mathrm{SynI}i} &= g_{\mathrm{SynI}}(v_i - v_{\mathrm{SynI}}) \textstyle\sum_{j=1, j\neq i}^{j=3} b_{ji} f(v_j), \\ I_{\mathrm{SynE}i} &= g_{\mathrm{SynE}}(v_i - v_{\mathrm{SynE}}) D_i, \end{aligned} \tag{2.2}$$

Copyright © by SIAM. Unauthorized reproduction of this article is prohibited.

Downloaded 09/04/22 to 130.49.198.139 . Redistribution subject to SIAM license or copyright; see https://epubs.siam.org/terms-privacy

Table 1

Parameter values for (2.1).

Parameter	Value	Parameter	Value	Parameter	Value	Parameter	Value
C	20 pF	g_{AD}	10 nS	v_{K}	-85 mV	g_{L}	2.8 nS
v_{L}	-60 mV	g_{SynI}	60 nS	v_{SynI}	-75 mV	g_{SynE}	10 nS
v_{SynE}	0 mV	v_{min}	-50 mV	v_{max}	-20 mV	τ_{AD}	2000 ms
K_{AD}	1	b_{21}	0.25	b_{31}	0.55	b_{12}	0.55
b_{32}	0.25	b_{13}	0.25	b_{23}	0.55	D_1	0.6
D_2	0.6	D_3	0.6				

where the b_{ji} are weight parameters that scale the baseline inhibitory conductance g_{SynI} and similarly the D_i scale the baseline excitatory conductance g_{SynE}. In general, the D_i allow for the introduction of heterogeneity among the neurons; in this work, we keep them equal. In (2.2), $f(v)$ is a voltage-sensitive piecewise smooth function, which provides a more analytically convenient approximation of a sigmoid function that allows synaptic output to grow with v up to a saturation level:

$$f(v) = \begin{cases} 0 & \text{if} \quad v < v_{\text{min}}, \\ (v - v_{\text{min}})/(v_{\text{max}} - v_{\text{min}}) & \text{if} \quad v_{\text{min}} \leq v < v_{\text{max}}, \\ 1 & \text{if} \quad v \geq v_{\text{max}}. \end{cases} \tag{2.3}$$

While I_{SynI} denotes inhibitory inputs, I_{SynE} represents a tonic synaptic excitation or drive such as may arise in CPG systems to adjust overall excitability or to provide a form of feedback signal.

Baseline model parameter values including coupling strengths are listed in Table 1. Note that each neuron is coupled to the two others and that the coupling is asymmetric, in that connections $b_{j,j+1}$, from neuron j to neuron $j+1$ (interpreted periodically) for each $j \in \{1, 2, 3\}$, are stronger than those from neuron $j+1$ to neuron j.

2.2. Basic activity patterns. With these parameter values and coupling properties, the neuronal network exhibits three types of activity patterns (Figure 1) depending on the inhibitory synaptic connection strength g_{SynI}. When $g_{\text{SynI}} = 60$, the network supports two stable solutions, one that we call smooth oscillations (SOs) (Figure 1(A)) and another that we name uphill relaxation oscillations (UROs) (Figure 1(B)). In addition to the substantial difference in their temporal voltage profiles, these two solutions show different orders of neuronal activation. Here we note that SOs follow the order of activation that the network would appear naturally to prefer under the given network architecture (Table 1). For example, suppose that neuron 1 is active. Parameter values in the model, particularly the coupling strengths, are set so that only one neuron is active, or at or near its voltage peak, at a time. Because neuron 1 is active and $b_{12} > b_{13}$, neuron 2 is more inhibited than neuron 3. Thus, as we see with SOs, once the voltage of neuron 1 peaks and decays, reducing the inhibition, neuron 3 has an advantage over neuron 2 and is able to activate next (Figure 1(A)). But this order is reversed in UROs (Figure 1(B)).

Copyright © by SIAM. Unauthorized reproduction of this article is prohibited.

Downloaded 09/04/22 to 130.49.198.139 . Redistribution subject to SIAM license or copyright; see https://epubs.siam.org/terms-privacy

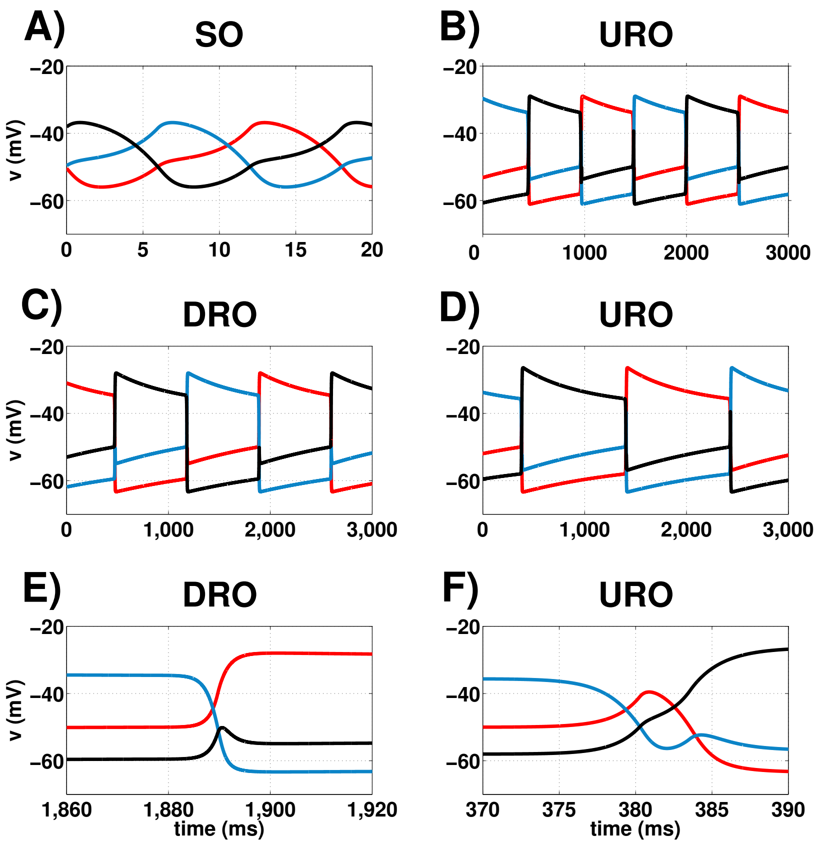

Figure 1. *The network demonstrates three types of activity patterns, SOs, UROs, and DROs. These activity patterns share the same set of parameters shown in Table* 1 *except* g_{SynI}. (A) *SOs when* $g_{\mathrm{SynI}} = 60$. (B) *UROs when* $g_{\mathrm{SynI}} = 60$. (C) *DROs when* $g_{\mathrm{SynI}} = 70$. (D) *UROs when* $g_{\mathrm{SynI}} = 70$. (E) *Temporal profile of transition in DROs shown in* (C). (F) *Temporal profiles of transition in UROs shown in* (D). *In all subfigures,* v_1 *is in red,* v_2 *in blue, and* v_3 *in black.*

If we increase g_{SynI} to 70, then we lose SOs in favor of another type of relaxation oscillation solution, which we call downhill relaxation oscillations (DROs). DROs follow the same, natural-seeming order of activation as SOs (Figure 1(C)). Under the same set of parameters for which DROs occur, a URO pattern also arises (Figure 1(D)), with a frequency much lower than that in Figure 1(B). In relaxation oscillations (either UROs or DROs), if a neuron is active, then its corresponding adaptation increases, hence its voltage decreases over time (equation (2.1)). Therefore, the amount of inhibition from the active neuron eventually decreases, allowing the suppressed neurons to depolarize over time until a switch of which neuron is active occurs. Figure 1(E) (1(F), resp.) shows a zoomed view of the temporal profiles of the neuronal voltages during the transition in Figure 1(C) (1(D), resp.). In both cases, as the voltage of neuron 2 comes down, both the voltages of neurons 1 and 3 rise but neuron 1 is less

Copyright © by SIAM. Unauthorized reproduction of this article is prohibited.

Downloaded 09/04/22 to 130.49.198.139 . Redistribution subject to SIAM license or copyright; see https://epubs.siam.org/terms-privacy

inhibited and correspondingly more depolarized. In DROs, the less-inhibited neuron 1 wins the competition with neuron 3 and activates next. In UROs, however, during the transition, the voltage of neuron 1 suddenly begins to decrease and neuron 3 wins. This sudden"turn-around" during a phase transition was also observed in previous work and appears to be a feature of the general model (2.1)–(2.2) [35] ("blip" in Figures 11, 12, and 13 in that paper).

2.3. Bifurcation diagrams. We numerically computed the bifurcation diagram for system (2.1), (2.2) using XPPAUT [14] with the inhibitory coupling parameter g_{SynI} as the bifurcation parameter and with two different forms of the coupling function f (Figure 2). In panels (A)

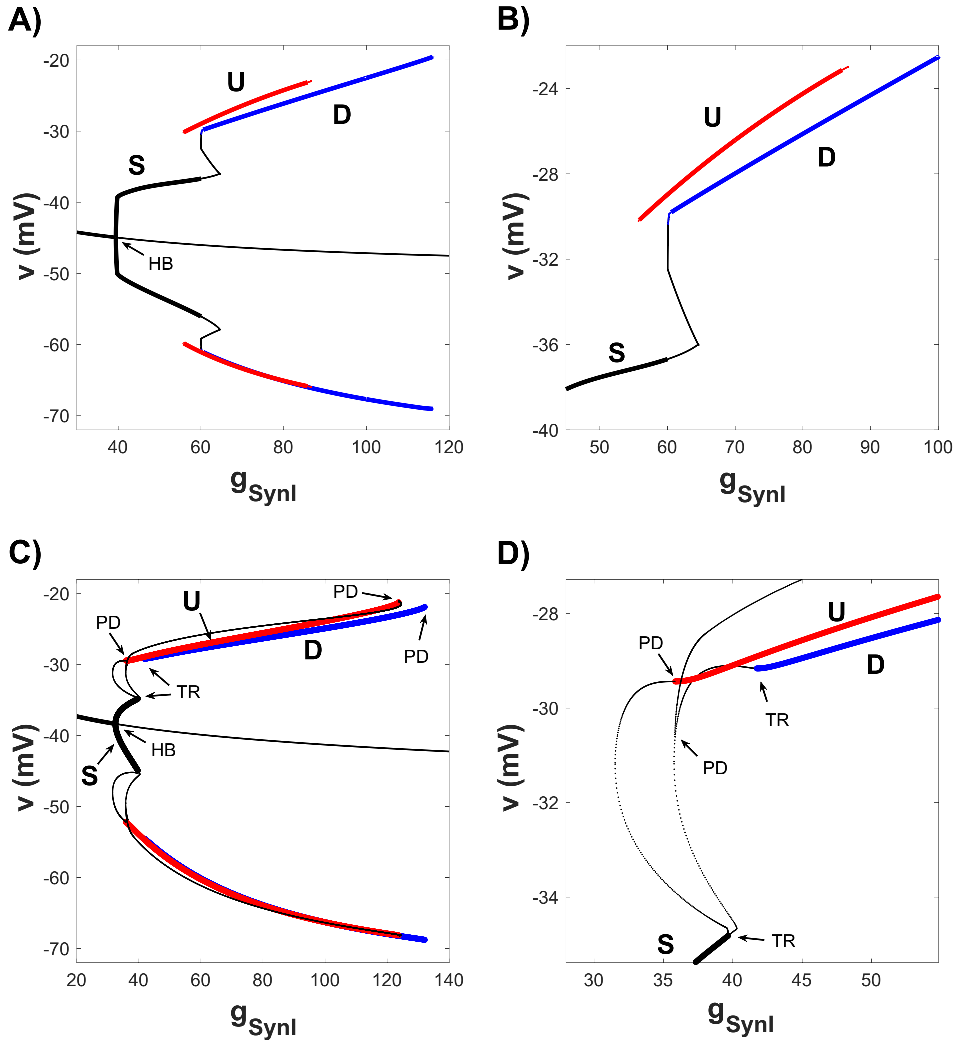

Figure 2. *Bifurcation diagram for the full model* (2.1), (2.2). (A), (B) *Full diagram and zoomed view when the coupling function is given by* (2.3). *Thick (thin) curves are stable (unstable) solutions. Black: SOs. Red: UROs. Blue: DROs.* (C), (D) *Full diagram and zoomed view for* $f(v) = 1/(1 + \exp(-(\mathrm{v} + 30)/4))$. *HB: Andronov–Hopf bifurcation. TR: torus bifurcation. PD: period doubling bifurcations. S: SOs. D: DROs. U: UROs.*

Copyright © by SIAM. Unauthorized reproduction of this article is prohibited.

Downloaded 09/04/22 to 130.49.198.139 . Redistribution subject to SIAM license or copyright; see https://epubs.siam.org/terms-privacy

and (C) of this diagram, the middle solid curve depicts the set of fixed points; the curve is thick where the fixed points are stable and thin where they are unstable. In both cases, the change of stability happens at an Andronov–Hopf bifurcation point (HB), from which a branch of stable SOs (S) emanates. For the coupling function given in (2.3) as shown in panel (A) and in a zoomed view in (B), we were unable to identify the bifurcation types at which the SOs destabilize for g_{SynI} just above 60. Separately, we were able to find and follow branches of stable DROs (blue) and UROs (red) and to locate points where they destabilized; in particular, we see that these solutions are bistable over a range of g_{SynI} values. With a smooth version of the coupling function, $f(v) = 1/(1 + \exp(-(\mathrm{v} + 30)/4))$, we generated a more complete diagram that matches the piecewise smooth case qualitatively. As shown in panel (C) and in a zoomed view in panel (D), in this case, the branch of stable SOs loses its stability at a torus bifurcation point (TR), where unstable branches of periodic solutions emerge. The unstable solutions become stable UROs (U, red) at a period doubling bifurcation (PD) and DROs (D, blue) at another torus bifurcation (TR), respectively. The latter two stable branches of relaxation oscillations terminate at PDs once g_{SynI} becomes sufficiently large. These more complete results suggest that similar bifurcation events induce changes in stability and give rise to similar unstable solution branches when coupling function (2.3) is used; additional evidence in support of this point will appear later in Figure 12.

To develop a better understanding of the bifurcation events underlying transitions related to UROs, we apply fast-slow decomposition. As done in past work [35], we generated a fast subsystem bifurcation diagram by treating the adaptation slow variables m_i as fixed parameters and studying fixed points of the three-dimensional system of v_i equations from (2.1)–(2.2). To do so, in XPPAUT, we integrate the full system over one full URO cycle (approximately 3 seconds; see Figure 1(D)) to generate a matrix M of slow variable values over the course of the cycle. A single auxiliary parameter, s, was introduced to parameterize the rows of the matrix M and to serve as a bifurcation parameter; the progression of s from 0 to 1 corresponds to one full oscillation cycle. Although the URO is associated with a specific trajectory in $(v_1, m_1, v_2, m_2, v_3, m_3)$-space, this method allows us to find all fixed points of the fast (v_1, v_2, v_3) equations present over the path taken in (m_1, m_2, m_3). Figure 3 shows the resulting bifurcation diagram for the v_i equations in (s, v_2)-space (black curves) along with the projection of the solution of the whole system (red dots). There are five fixed points when $s = 0$, the upper- and lowermost of which are stable (thicker black curves). As s increases, fixed point branches arise and disappear in pairs, via saddle-node bifurcations, with three stable branches present for much of the range of s.

Next, we consider the projection of the trajectory of the full system (red). At time 0, corresponding to $s = 0$, v_2 is elevated, and as s increases from 0, the trajectory moves along the upper branch of stable fixed points. A saddle-node bifurcation occurs around $s = 0.25$, where two upper branches of fixed points merge together and disappear. Once this happens, the voltage of neuron 2 stays nearby for a while and then drops sharply and converges to another branch of stable fixed points at a lower v_2 value below v_{min}. As s increases further, the two upper fixed point branches reappear through another saddle-node bifurcation. Subsequently, the middle branch where the trajectory had settled is lost in its own saddle-node bifurcation. Beyond this bifurcation point, there are two stable fixed point branches, one at elevated v_2 and one at more hyperpolarized v_2. The voltage of neuron 2 initially rises toward the upper branch

Downloaded 09/04/22 to 130.49.198.139 . Redistribution subject to SIAM license or copyright; see https://epubs.siam.org/terms-privacy

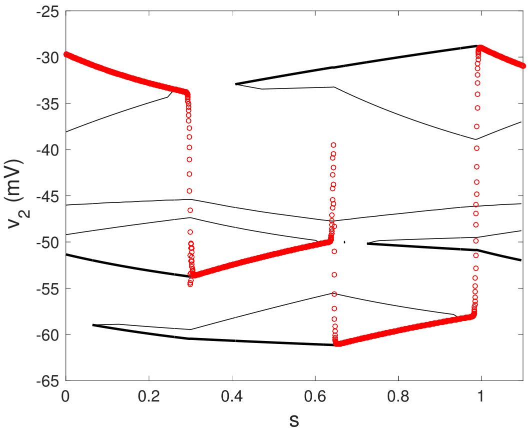

Figure 3. *Bifurcation diagram of the fast system associated with UROs projected onto* (s, v_2)*-space. Black: fixed point curves for the* (v_1, v_2, v_3) *equations (thick: stable; thin: unstable). Red: projection of the solution of the full system* (2.1), (2.2).

but for some reason, it turns around and settles on the lowest branch of stable fixed points in (s, v_2)-space. Last, this branch undergoes another saddle-node bifurcation and the voltage of neuron 2 rises quickly to complete the cycle of the activity pattern shown in Figure 1(D).

From this analysis, we observe that saddle-node bifurcations of fast subsystem fixed points are implicated in initiating the transitions between phases within a URO cycle. Standard fast-slow analysis would provide transition surfaces where these bifurcations occur, as a function of the slow variables. It is not clear, however, what factors determine whether UROs or DROs arise for a given set of parameters and initial conditions and what causes the "turn-around" in UROs. We next turn to a linear simplification of our model system on which we can perform additional analysis. We shall see that to address some of these questions, we will need to consider the fast subsystem together with the slow subsystem to determine the outcomes of phase transitions.

3. Linear model.

In standard fast-slow analysis, the starting point is to determine the set of fixed points of the fast subsystem. Due to the voltage-sensitive coupling described in (2.3), the voltage equations from system (2.1), (2.2) have only isolated fixed points, and these depend on where each voltage variable lies relative to $\{v = v_{min}\}$ and $\{v = v_{max}\}$. Moreover, we find that a complication arises due to the proximity of the voltage nullsurfaces in certain regions of (v_1, v_2, v_3)-space, which can blur the distinction between fast and slow timescales. We therefore turn to a simplified linear model setting in which we can perform analysis that is useful for revealing what factors determine which solution types exist and are stable as well as what mechanism causes the apparent turn-around during some phase transitions.

Although we cannot derive the linear model rigorously from the full model, we can provide numerical and heuristic analytical justifications for this simplification. Numerically, it appears to exhibit similar behavior to the full model; we shall see that the bifurcation analysis for the three-cell version of this model, presented in Figure 12, agrees qualitatively with the full model diagram (Figure 2) including the extra details that we were able to flesh out using a smooth

Copyright © by SIAM. Unauthorized reproduction of this article is prohibited.

Downloaded 09/04/22 to 130.49.198.139 . Redistribution subject to SIAM license or copyright; see https://epubs.siam.org/terms-privacy

coupling function (Figure 2(C), (D)). Analytically, we note that for the relaxation oscillations on which we focus, each v_i is approximately constant in each active and silent phase, and each unit is usually in the silent phase while it is inhibited. Thus, the $(v_i - v_{SynI})$ term in I_{SynI} to leading order acts as a constant factor when the term $f(v_j)$ that it multiplies is nonzero. For the product $m_i(v_i - v_K)$ in I_{ADi}, $(v_i - v_K)$ is approximated by a larger constant when unit i is active and by a smaller constant when it is silent. The larger constant reduces the size to which m_i must grow to induce a fixed negative feedback on v_i. The smaller constant allows adaptation to wear off even at larger m_i values. Together, these effects compress the range of m_i over each oscillation, but they are not expected to cause a qualitative change in dynamics. Finally, both v_i and $K_{AD}f(v_i)$ are monotone increasing functions, yielding qualitatively similar m_i dynamics across the two models.

For the linear analysis, we begin with a two-neuron network and focus on the three-neuron network afterward. Although the two-neuron network cannot demonstrate all of the activity patterns observed in the full model, its dynamics include some important features of the relaxation oscillation dynamics in the full model and hence this initial analysis will help us to understand the mechanisms involved.

3.1. Two-neuron network.

Here we consider the following system:

$$\begin{aligned} \dot{v}_i &= I - v_i - m_i - gf(v_j), \\ \dot{m}_i &= \epsilon(v_i - am_i), \end{aligned} \tag{3.1}$$

where $i \in \{1, 2\}$, $j = 3 - i$, and $f(v)$ is the same function given in (2.3). We use g as a bifurcation parameter and fix the other parameter values as $a = 2$, $I = 6$, $\epsilon = 0.01$, $v_{\min} = 0$, and $v_{\max} = 5$ throughout the remainder of this paper unless otherwise specified. To find critical points of the full system (3.1), we need to solve the following system of equations:

$$\begin{cases} I - v_1 - v_1/a - gf(v_2) &= 0, \\ I - v_2 - v_2/a - gf(v_1) &= 0. \end{cases} \tag{3.2}$$

We refer to the two curves defined by these equations as the v-nullclines, although the general v_i-nullcline is parameterized by m_i, whereas here m_i is fixed at v_i/a. These curves are symmetric about the identity line and are each composed of three linear parts with two elbows, or points where the slope changes, since $f(v)$ is a piecewise linear function (Figure 4). Figure 4 also shows the two elbows of the v_1-nullcline, defined by the first equation in (3.2), which are given by $(a(I - g)/(a + 1), v_{\max})$ and $(aI/(a + 1), v_{\min})$ (red dots). Note that the latter does not depend on g. With this elbow fixed, we may obtain one or three fixed points of system (3.1) depending on g (Figure 4). When the slope of the middle branch of the v_1-nullcline becomes -1, there are infinitely many fixed points. This happens when $g = v_{\max}(a + 1)/a = 7.5$. In summary, there is only one fixed point in the system if $g < 7.5$ and there are three fixed points if $g > 7.5$.

Now, assume that there is a critical point (v_1, v_2) with $v_1 = v_2 < v_{\min} = 0$. Figure 4 suggests that this type of critical point does not exist. Indeed, if $v_1 = v_2 < v_{\min} = 0$, we obtain $v_i = aI/(a + 1)$ from (3.2), which contradicts the assumption $v_i < v_{\min} = 0$. Now, consider a critical point (v_1, v_2) with $v_1 < v_{\min}$ and $v_2 \in (v_{\min}, v_{\max})$ or $v_2 < v_{\min}$ and $v_1 \in (v_{\min}, v_{\max})$ as shown in Figure 4(A).

Copyright © by SIAM. Unauthorized reproduction of this article is prohibited.

Downloaded 09/04/22 to 130.49.198.139 . Redistribution subject to SIAM license or copyright; see https://epubs.siam.org/terms-privacy

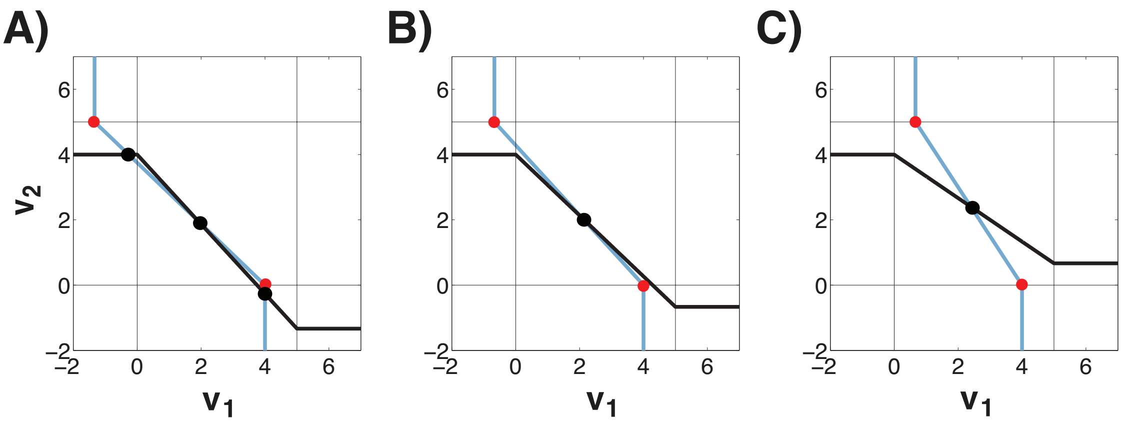

Figure 4. *v-nullclines for system* (3.1) *with* $m_i = v_i/a$. *The* v_1*-nullcline appears in blue and the* v_2*-nullcline in black. Red dots denote elbows of the* v_1*-nullcline, where it changes slope. Black dots are critical points.* (A) $g = 8$, (B) $g = 7$, (C) $g = 5$.

Proposition 3.1. *The system* (3.1) *has two stable critical points,* (v_1, v_2)*, with either* $v_1 < v_{\min}$ *and* $v_2 \in (v_{\min}, v_{\max})$ *or* $v_2 < v_{\min}$ *and* $v_1 \in (v_{\min}, v_{\max})$*, for* $g > 7.5$.

Proof. Due to the symmetry of system (3.1), it is enough to find a stable critical point (v_1, v_2) with $v_1 < v_{\min}$ and $v_2 \in (v_{\min}, v_{\max})$. Since $f(v_1) = 0$ and $f(v_2) = (v_2 - v_{\min})/v_{\max}$ under this assumption on v_1 and v_2, equations (3.2) yield $v_2 = aI/(a+1)$ and we use this to solve for v_1, which yields $v_1 = a(I - \gamma)/(a+1)$ where

$$\gamma := g\left(\frac{aI/(a+1) - v_{\min}}{v_{\max} - v_{\min}}\right).$$

Now, we require $v_1 < v_{\min}$ for consistency and obtain the condition $g > 7.5$. To determine the stability of this critical point, we linearize the system of equations (3.1) around this point and find that this matrix has two repeated negative eigenvalues,

$$\lambda = \frac{-(a\epsilon + 1) \pm \sqrt{(a\epsilon + 1)^2 - 4(a+1)\epsilon}}{2}.$$

Thus, the critical point is stable. ■

Now consider a fixed point (v_1, v_2) with both $v_1, v_2 \in (v_{\min}, v_{\max})$. Due to the symmetry of the system (3.1), $v_1 = v_2$ and we have the following result regarding the existence and stability of this fixed point.

Proposition 3.2. *The system* (3.1) *has a critical point,* (v_1, v_2)*, with* $v_1 = v_2 \in (v_{\min}, v_{\max})$ *for each* $g > 0$*. This critical point is stable only for* $g < v_{\max}(1 + a\epsilon)$*, which gives* $g < 5.1$ *for our default parameter values.*

Proof. Under the assumption that $v_1 = v_2 \in (v_{\min}, v_{\max})$, we obtain $v_i = aIv_{\max}/(av_{\max} + ag + v_{\max})$ from the system (3.1), which is always less than $v_{\max}$ for all positive g. Now, we

Copyright © by SIAM. Unauthorized reproduction of this article is prohibited.

linearize the system (3.1) around this point and obtain a Jacobian matrix with characteristic polynomial

$$\left\{\lambda^2 + (1 + a\epsilon + G)\lambda + \epsilon(a + 1 + aG)\right\}\left\{\lambda^2 + (1 + a\epsilon - G)\lambda + \epsilon(a + 1 - aG)\right\} = 0,$$

where $G = g/v_{\max}$. From the first factor of this polynomial, we compute

$$\lambda_{1,2} = \frac{-(1 + a\epsilon + G) \pm \sqrt{(1 + a\epsilon + G)^2 - 4\epsilon(a + 1 + aG)}}{2}.$$

Obviously, $\lambda_{1,2}$ are either two negative reals or two complex numbers with negative real parts. On the other hand, from the second factor of this polynomial, we obtain

$$\lambda_{3,4} = \frac{-(1 + a\epsilon - G) \pm \sqrt{(G + a\epsilon - 1 + 2\sqrt{\epsilon})(G + a\epsilon - 1 - 2\sqrt{\epsilon})}}{2}.$$

First, note that for $v_{\max}(1 - a\epsilon - 2\sqrt{\epsilon}) < g < v_{\max}(1 - a\epsilon + 2\sqrt{\epsilon})$ or $3.9 < g < 5.9$, $\lambda_{3,4}$ are complex eigenvalues. Second, the quantity $1 + a\epsilon - G$ changes its sign from positive to negative as g crosses $v_{\max}(1 + a\epsilon) = 5.1$. Thus, for $3.9 < g < 5.1$, $\lambda_{3,4}$ are two complex eigenvalues with negative real parts; for $5.1 < g < 5.9$, they are two complex eigenvalues with positive real parts; and last, for $g > 5.9$, they are two positive real eigenvalues. ■

Figure 5(A) shows a numerically computed bifurcation diagram for system (3.1), which confirms our analysis. Note that by symmetry, we obtain the same diagram in (g, v_1) and in (g, v_2), so we simply label the vertical axis with v. The middle branch in the diagram consists of the set of fixed points with $v_1 = v_2 \in (v_{\min}, v_{\max})$. For $g < 5.1$, it is stable and denoted by a thick curve. At $g = 5.1$, when it loses stability (thin curve), stable relaxation oscillations emerge and persist until $g = 7.5$. An example of the relaxation oscillation solution when $g = 6$ is shown in Figure 5(B). For $g > 7.5$, there are three fixed points, and the two asymmetric ones are stable.

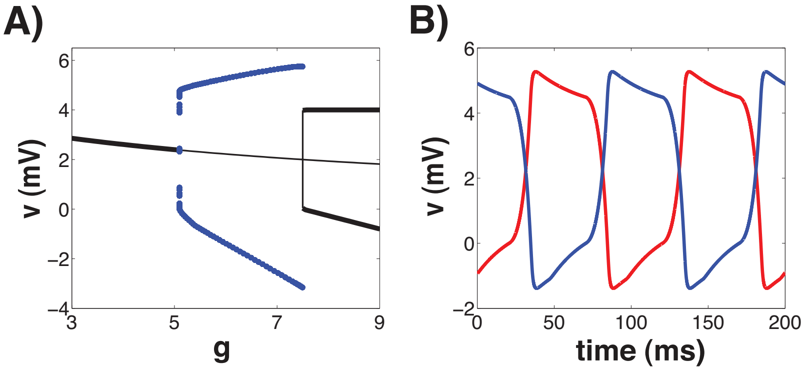

Figure 5. (A) *Bifurcation diagram of system* (3.1) *with* g *as a bifurcation parameter. Stable (unstable) fixed points are denoted by thick (thin) black curves. Blue dots represent the maximum and minimum values of* v *in relaxation oscillations.* (B) *Activity patterns of system* (3.1) *when* $g = 6$. v_1 *is in red and* v_2 *in blue.*

Copyright © by SIAM. Unauthorized reproduction of this article is prohibited.

Downloaded 09/04/22 to 130.49.198.139 . Redistribution subject to SIAM license or copyright; see https://epubs.siam.org/terms-privacy

Downloaded 09/04/22 to 130.49.198.139 . Redistribution subject to SIAM license or copyright; see https://epubs.siam.org/terms-privacy

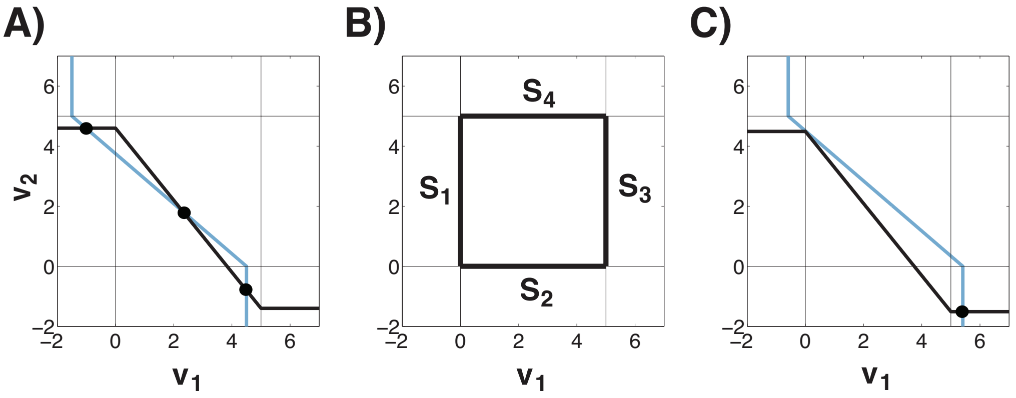

Figure 6. *Nullclines of v_i with m_i as parameter. In* (A) *and* (C)*, the v_1-nullcline is in blue and the v_2-nullcline is in black.* (A) *$g = 6$, $m_1 = 1.5$, and $m_2 = 1.4$.* (B) *Transitions in the nature of the critical points can only can happen on the thick lines, S_1-S_4, where one of the v_i is in the set $\{v_{min}, v_{max}\}$.* (C) *One example of the v-nullclines at a transition that happens on the line segment S_1.*

Next, utilizing the fact that v_i $(i = 1, 2)$ are fast variables and m_i $(i = 1, 2)$ are slow variables, we perform a fast-slow analysis to study relaxation-type oscillations in system (3.1) for $g > 5.1$. We call the system of fast variables the fast subsystem and slow variables the slow subsystem. The idea here is that we first treat m_i $(i = 1, 2)$ as parameters to determine the attractors of the fast subsystem and the transition curves in (m_1, m_2)-parameter space where bifurcations occur for the fast subsystem. Second, we consider how, once the fast subsystem has settled to an attractor, the dynamics of the slow subsystem, with m_i $(i = 1, 2)$ as dynamic variables, can cause the attractor structure to change and potentially induce a fast jump to a new attractor.

Note that the nullclines of the fast variables v_i $(i = 1, 2)$ are given by

$$v_i = I - m_i - gf(v_j), \tag{3.3}$$

where $j = 3-i$. While there is only one fixed point in the whole system for $g < 7.5$ (Figure 4), when we treat m_i $(i = 1, 2)$ as parameters, the fast subsystem can have more than one fixed point. Figure 6(A) shows one example with two stable fixed points and one unstable fixed point of the fast subsystem when $g = 6$, $m_1 = 1.5$, and $m_2 = 1.4$.

As in the full model case (e.g., Figure 3), we find that the transitions between fast subsystem attractors are triggered by saddle-node bifurcations. Due to the geometry of the v_i-nullclines, these bifurcations can arise only on the four line segments, S_1–S_4, shown in Figure 6(B) (thick lines). In fact, as we shall show later, with the baseline set of parameters, the bifurcation can happen only on S_1 and S_2. First, we find the condition for the bifurcation to occur on the line segment S_1. For this bifurcation, the elbow of the v_2-nullcline, $(0, I - m_2)$, should lie on the line segment S_1 and, at the same time, on the middle branch of the v_1-nullcline, $v_1 = -gv_2/v_{\max} + I - m_1$ (Figure 6(C)). Thus, given that $v_{min} = 0$, we see that the following two conditions must hold:

$$\Sigma_1 : \qquad I - v_{\max} < m_2 < I \quad \text{and} \quad m_1 = \frac{g}{v_{\max}} m_2 + I\left(1 - \frac{g}{v_{\max}}\right).$$

Copyright © by SIAM. Unauthorized reproduction of this article is prohibited.

Downloaded 09/04/22 to 130.49.198.139 . Redistribution subject to SIAM license or copyright; see https://epubs.siam.org/terms-privacy

In other words, a fast subsystem saddle-node bifurcation transition occurs on the line segment S_1 when the slow variables satisfy Σ_1. The conditions Σ_1 define a curve in (m_1, m_2)-space, which we call a transition curve. Similarly, we can find other transition curves, corresponding to fast subsystem saddle-node bifurcations on the line segments S_2, S_3, and S_4 as follows:

$$\begin{aligned}
\Sigma_2 :& I - v_{\max} < m_1 < I \quad \text{and} \quad m_2 = \frac{g}{v_{\max}} m_1 + I\left(1 - \frac{g}{v_{\max}}\right),\\
\Sigma_3 :& I - g - v_{\max} < m_2 < I - g \quad \text{and} \quad m_1 = -\frac{g}{v_{\max}}(I - m_2 - g) + I - v_{\max},\\
\Sigma_4 :& I - g - v_{\max} < m_1 < I - g \quad \text{and} \quad m_2 = -\frac{g}{v_{\max}}(I - m_1 - g) + I - v_{\max}.
\end{aligned}$$

Now we can treat m_i $(i = 1, 2)$ as dynamic variables in the full model and describe how a transition from the v_1-on state $(v_1 > v_{max})$ to the v_2-on state $(v_2 > v_{max})$ happens (Figure 7). Figure 7(A) shows time courses of v_1 (blue) and v_2 (black) and Figure 7(B) time courses of m_1 (blue) and m_2 (black). Some time points marked with dots in Figures 7(A)–(B) are illustrated in the subsequent panels. Figure 7(C) shows the (v_1, v_2) fast phase plane with the v_i-nullclines and a projection of the attracting solution at a moment in time when $v_1 = v_{max}$ with $v_2 < v_{min}$ (red dot). Figure 7(H) shows the corresponding projected solution onto the slow phase-plane (red dot, point C). In the v_1-on state, m_1 increases and m_2 decreases based on (3.1). In the fast phase plane, this means that the v_1-nullcline moves leftward and the v_2-nullcline moves upward. In the slow phase plane, on the other hand, the projected solution moves to the lower right. Once it hits the transition curve Σ_2 in the slow phase plane (Figure 7(H), point D), the stable fixed point is lost through a saddle-node bifurcation in the fast phase plane (Figure 7(D)) and the projected trajectory moves to the other stable fixed point and settles down there (Figures 7(E)–(G)), corresponding to the v_2-on state. During this transition, the projected solution in the slow phase plane slowly turns around and moves to the upper left. Now this process repeats in the v_2-on state.

Figure 8 shows the slow phase plane with transition curves and the projected solution for various g (from the left to the right, $g = 7, 6$, and 5.1). In all panels, Σ_1 (Σ_2) is given by the upper (lower) dashed black curve. When $g = 5.1$ (Figure 8(C)), Σ_3 (lower solid black curve) and Σ_4 (upper solid black curve) appear from the lower left corner, while for the other g values, no points in the (m_1, m_2)-plane satisfy the conditions for Σ_3, Σ_4. The red curves denote the projections of attracting trajectories of the full system (3.1). As explained in the previous paragraph, whenever the projected trajectory hits one of the transition curves, the stable fixed point is lost through a saddle-node bifurcation and the trajectory quickly approaches the other fixed point. As a result, the projected trajectory in (m_1, m_2)-space turns around. For large g, this turn-around happens shortly after the bifurcation. For small g, however, it takes longer to turn around because the two v_i-nullclines are close to each other in the fast phase plane; this phenomenon of slowing just beyond a saddle-node bifurcation is sometimes referred to as the effect of the ghost of the lost fixed points.

Finally, we show that for our current parameters, after an initial transient, fast subsystem bifurcations can happen only on the line segments S_1 and S_2, corresponding to the slow variables crossing through Σ_1, Σ_2 but not through Σ_3, Σ_4. Consider the partitioning of (v_1, v_2)-

Copyright © by SIAM. Unauthorized reproduction of this article is prohibited.

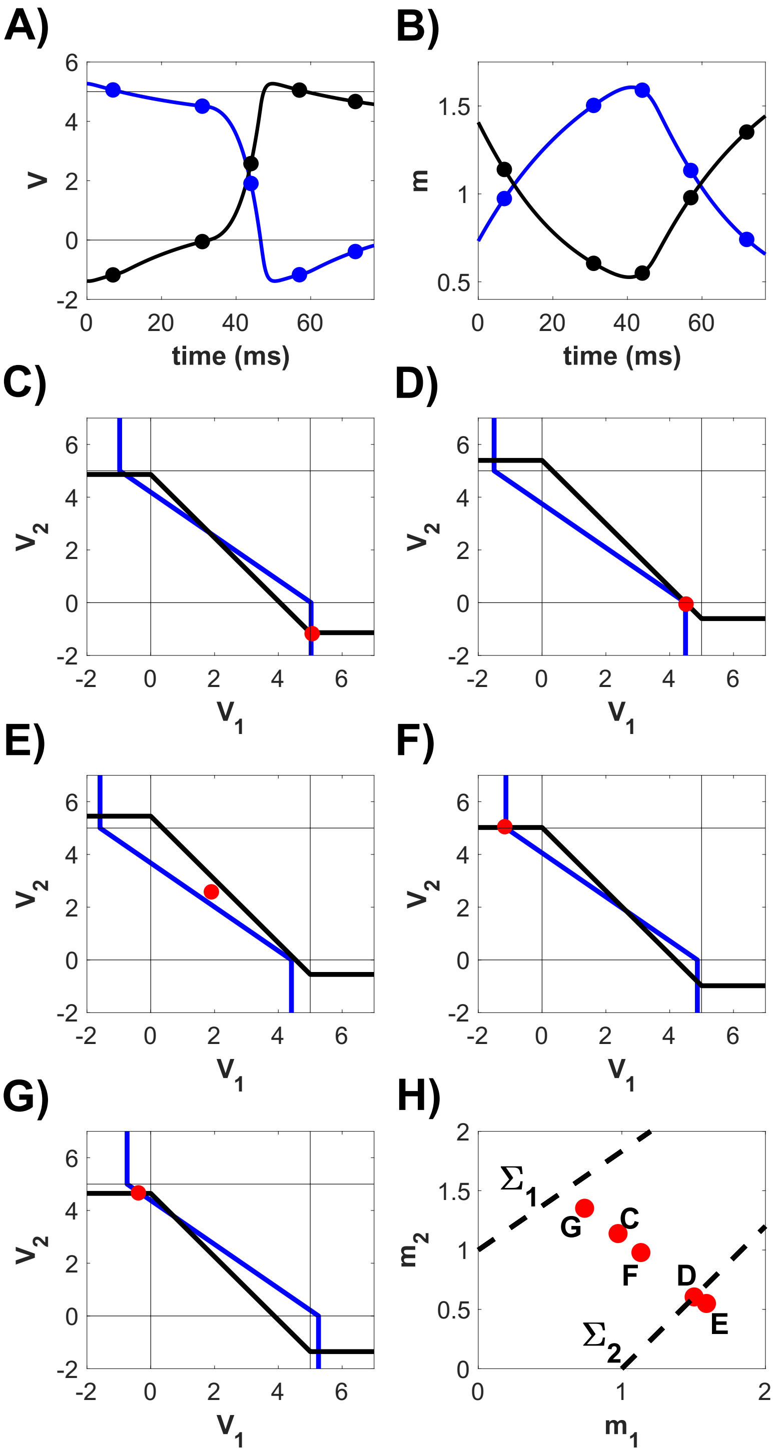

Figure 7. (A)–(G)*: The transition from* v_1*-on state to* v_2*-on state in the fast subsystem when* $g = 6$*.* (A) *Time courses of* v_1 *(blue) and* v_2 *(black).* (B) *Time courses of* m_1 *(blue) and* m_2 *(black).* (A)–(B) *Time points marked with dots are illustrated in the subsequent panels, in order from earliest time to latest time.* (C)–(G) *Each panel shows the projection of full model trajectory (red) along with the* v_1 *nullcline (blue) and* v_2 *nullcline (black).* (H) *The transition in the slow subsystem. When the projected solution hits one of the transition curves (*Σ_2*), a saddle-node bifurcation occurs in the fast subsystem (e.g., panel* (D)*).*

Downloaded 09/04/22 to 130.49.198.139 . Redistribution subject to SIAM license or copyright; see https://epubs.siam.org/terms-privacy

Copyright © by SIAM. Unauthorized reproduction of this article is prohibited.

Downloaded 09/04/22 to 130.49.198.139 . Redistribution subject to SIAM license or copyright; see https://epubs.siam.org/terms-privacy

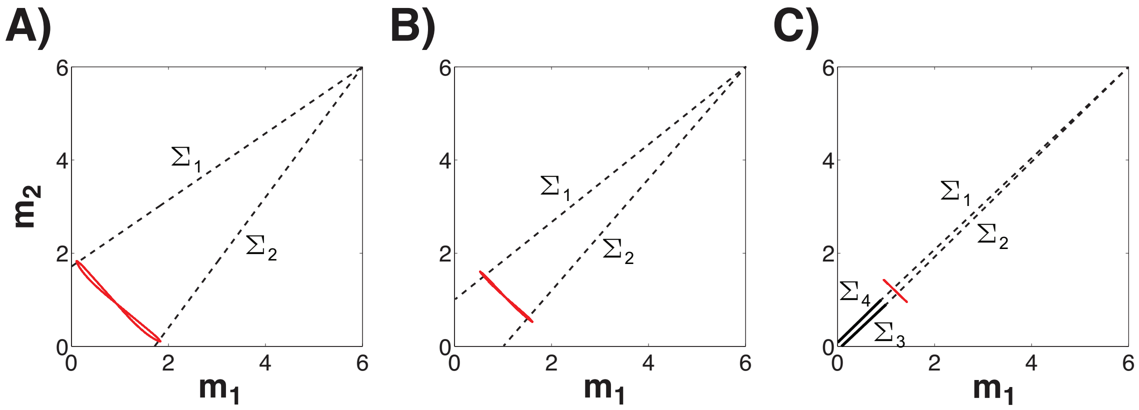

Figure 8. *Transition curves. From left to right, $g = 7, 6,$ and 5.1. In each figure, upper dashed black curve denotes transition curve on the line segment S_1 (Σ_1), lower dashed black curve on S_2 (Σ_2), lower solid black curve on S_3 (Σ_3), and upper solid black curve on S_4 (Σ_4). Red curves in each figure denote projection of the trajectories of the full model under corresponding g values.*

space shown in Figure 6(B). We define the following six regions: $P = \{(v_1, v_2) : 0 < v_1 < v_{max}, v_2 < 0\}, Q = \{(v_1, v_2) : v_1 > v_{max}, v_2 < 0\}, R = \{(v_1, v_2) : v_1 > v_{max}, 0 < v_2 < v_{max}\}$, and $\bar{P}, \bar{Q}, \bar{R}$ defined analogously but with the roles of v_1 and v_2 reversed (Figure 9(A)). Note that region Q is bounded by two rays: $\alpha := \{v_1 = v_{max}, v_2 \leq 0\}$ and $\beta := \{v_1 \geq v_{max}, v_2 = 0\}$. Similarly, $\bar{Q}$ is bounded by the two rays $\bar{\alpha} := \{v_2 = v_{max}, v_1 \leq 0\}, \bar{\beta} := \{v_2 \geq v_{max}, v_1 = 0\}$.

Since the v_i-nullclines are defined by (3.3), the region in which they intersect depends on m_1, m_2. Indeed, we can partition (m_1, m_2)-space into corresponding regions with the same names, such that the v_i-nullclines intersect in region X in (v_1, v_2)-space if and only if (m_1, m_2) lie in region X in (m_1, m_2)-space (Figure 9(B)). Similarly, (3.3) and the definition of f yield rays in (m_1, m_2)-space corresponding to those in (v_1, v_2)-space: $\alpha := \{m_1 = I - v_{max}, m_2 > I - g\}$ and $\beta, \bar{\alpha}, \bar{\beta}$ defined analogously. The kite bounded by $\Sigma_1, \Sigma_2, \Sigma_3, \Sigma_4$ is partitioned into seven regions by $\alpha, \beta, \bar{\alpha}, \bar{\beta}$; these regions also correspond to seven of the possible intersections $P \cap \bar{P}, P \cap \bar{Q}, \dots, R \cap \bar{R}$, although the two intersections $P \cap \bar{R}$ and $R \cap \bar{P}$ are empty and hence not among these regions (Figure 9(C)). Trajectories that leave the kite from region $P \cap \bar{Q}$ by passing through Σ_2, for example, start in P and end up in $\bar{Q}$. Finally, we note that the line connecting the boundary point $(m_1, m_2) = (I - v_{max}, I - g)$ between Σ_2 and Σ_3 to the boundary point $(m_1, m_2) = (I - g, I - v_{max})$ between Σ_1 and Σ_4, which we will call $\mathcal{L}$, has slope -1 and takes the form $m_2 = -m_1 + 2I - g - v_{max}$.

From region P, trajectories pass through Σ_2, since $\dot{m}_1 > 0$ on α, $\dot{m}_2 < 0$ in P, $\dot{m}_1 > 0$ on the part of Σ_2 with $m_1 < I/(a+1)$, and there are no critical points of the (m_1, m_2) dynamics in P. Moreover, from region Q, trajectories pass into P or R. Thus, it suffices to consider the fate of trajectories from R. In region R, the fixed point of the fast subsystem is given by

$$\begin{aligned} v_1 &= I - m_1 - g(I - m_2 - g)/v_{max}, \\ v_2 &= I - m_2 - g. \end{aligned}$$

Copyright © by SIAM. Unauthorized reproduction of this article is prohibited.

Downloaded 09/04/22 to 130.49.198.139 . Redistribution subject to SIAM license or copyright; see https://epubs.siam.org/terms-privacy

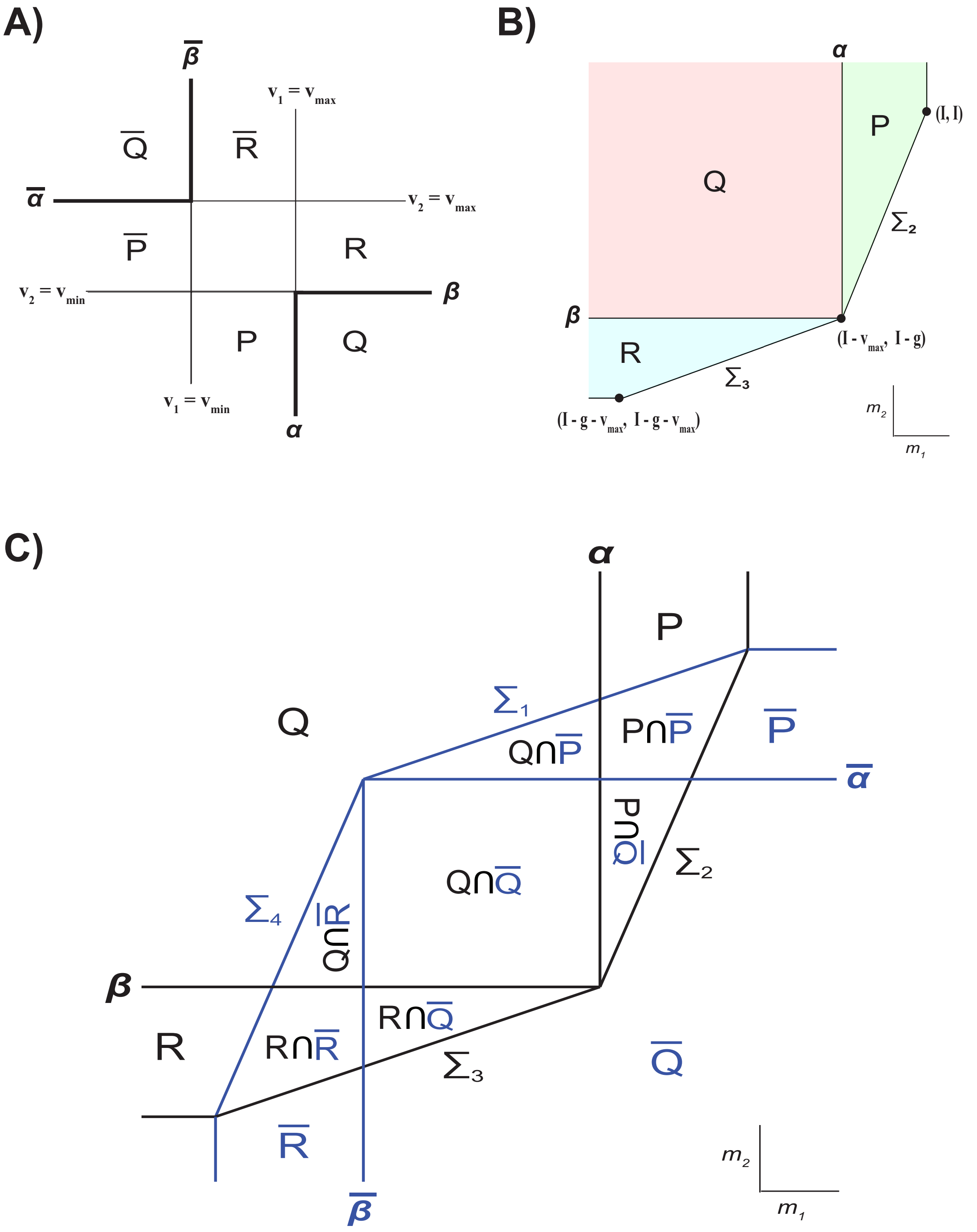

Figure 9. *Key transition curves and the regions they bound.* (A) *Partition of* (v_1, v_2)*-space.* (B) *Regions* P*,* Q*, and* R *in* (m_1, m_2)*-space.* (C) *All six regions in* (m_1, m_2)*-space.*

Copyright © by SIAM. Unauthorized reproduction of this article is prohibited.

Downloaded 09/04/22 to 130.49.198.139 . Redistribution subject to SIAM license or copyright; see https://epubs.siam.org/terms-privacy

Hence, the slow subsystem is

$$\begin{aligned} \dot{m}_1 &= I - m_1 - g(I - m_2 - g)/v_{max} - am_1, \\ \dot{m}_2 &= I - m_2 - g - am_2. \end{aligned} \tag{3.4}$$

From system (3.4), we can deduce two results about the vector field for sufficiently large g. First, the vector field points from R into Q on the boundary β between the two regions, where $m_2 = I - g$. Second, on Σ_3, we have $\dot{m}_1 = v_m - am_1 > 0$ and an algebraic calculation shows that the slope of the vector field, dm_2/dm_1, exceeds the slope v_m/g of Σ_3, such that the vector field points into R from Σ_3 as long as g is sufficiently large. Indeed, expressing m_2 as a function of m_1 on Σ_3 based on the definition of Σ_3 reveals that the highest order term in g in dm_2/dm_1 along Σ_3 is $ag > 0$, while v_m/g goes to 0 for large g. Hence, no trajectories leave through Σ_3. For smaller g, however, the vector field points out along at least part of Σ_3. Trajectories that leave through Σ_3 end up in $\bar{R}$ or $\bar{Q}$; in the latter case, they next pass into either $\bar{R}$ or $\bar{P}$.

Given these properties, to achieve the desired result, since $\dot{m}_1 > 0$ in R and Q, it suffices to show that $dm_2/dm_1 > -1$ in R as well as in the part of Q below the boundary line $\mathcal{L}$ between the upper half of the kite bounded by Σ_1, Σ_2 and the lower half bounded by Σ_3, Σ_4; this part of Q is specified by the condition

$$m_2 \leq -m_1 + 2I - g - v_{max}. \tag{3.5}$$

If these results hold, then $dm_2/dm_1 < -1$ will hold analogously in $\bar{R}$. Together, these properties of the vector field will ensure that leaving the kite through Σ_3 (and similarly Σ_4) can be at most transient; over successive cycles, trajectories that do so will be forced closer to and then across $\mathcal{L}$, such that eventually either (1) a cycle occurs such that when v_1 is on, the trajectory leaves the kite by reaching Σ_2, or (2) a cycle occurs such that when v_2 is on, the trajectory leaves the kite by reaching Σ_1. In either case, all subsequent fast subsystem bifurcations will occur when (m_1, m_2) reach $\Sigma_1 \cup \Sigma_2$.

An algebraic calculation starting from (3.4) shows that $dm_2/dm_1 > -1$ in R if and only if

$$m_2(g/v_{max} - (1 + a)) > g - 2I + (I - g)g/v_{max} + m_1(1 + a),$$

where $g/v_{max} - (1 + a)$ is negative for our parameters. Based on the definition of R, in the worst case, $m_2 = I - g$ and $m_1 = I - v_{max}$, such that this inequality is equivalent to the condition $a(g - I) > aI - v_{max}(1 + a)$, or

$$g > 2I - v_{max}(1 + a)/a. \tag{3.6}$$

The right-hand side of expression (3.6) is 4.5 for our parameter set, so the desired result holds since we only consider $g > 5$. In Q, we have

$$\begin{aligned} \dot{m}_1 &= I - m_1(1 + a), \\ \dot{m}_2 &= I - g - m_2(1 + a). \end{aligned}$$

Copyright © by SIAM. Unauthorized reproduction of this article is prohibited.

Downloaded 09/04/22 to 130.49.198.139 . Redistribution subject to SIAM license or copyright; see https://epubs.siam.org/terms-privacy

The desired condition $dm_2/dm_1 > -1$ becomes

$$m_1(1+a) < 2I - g - m_2(1+a).$$

In the relevant region, the worst case occurs when m_2 is as large as possible, which, based on (3.5), is $m_2 = -m_1 + 2I - g - v_{max}$. Thus, it suffices to have $v_{max}(1+a) - a(2I-g) > 0$, or $g > 2I - v_{max}(1+a)/a$. But this is exactly condition (3.6), which we have already confirmed for our parameter set.

We illustrate this trajectory behavior in Figure 10. Figure 10(A) shows the typical trajectory behavior for g sufficiently large. In this case, the vector field points into R from Σ_3, hence no trajectory leaves through Σ_3. In Figure 10(B) ($g = 6.2$), the trajectory leaves R through Σ_3 and ends up in $\bar{Q}$. In this case, the trajectory next passes into $\bar{P}$ and leaves $\bar{P}$ through Σ_1. In Figure 10(C) ($g = 5.5$), the trajectory leaving R through Σ_3 ends up in $\bar{Q}$, then passes into $\bar{R}$ and then leaves $\bar{R}$ through Σ_4. After this, it passes from Q to P and leaves through Σ_2. Finally, in Figure 10(D) ($g = 5.5$, with a different initial condition from the previous case), the trajectory in Q passes into R through β and then leaves R through

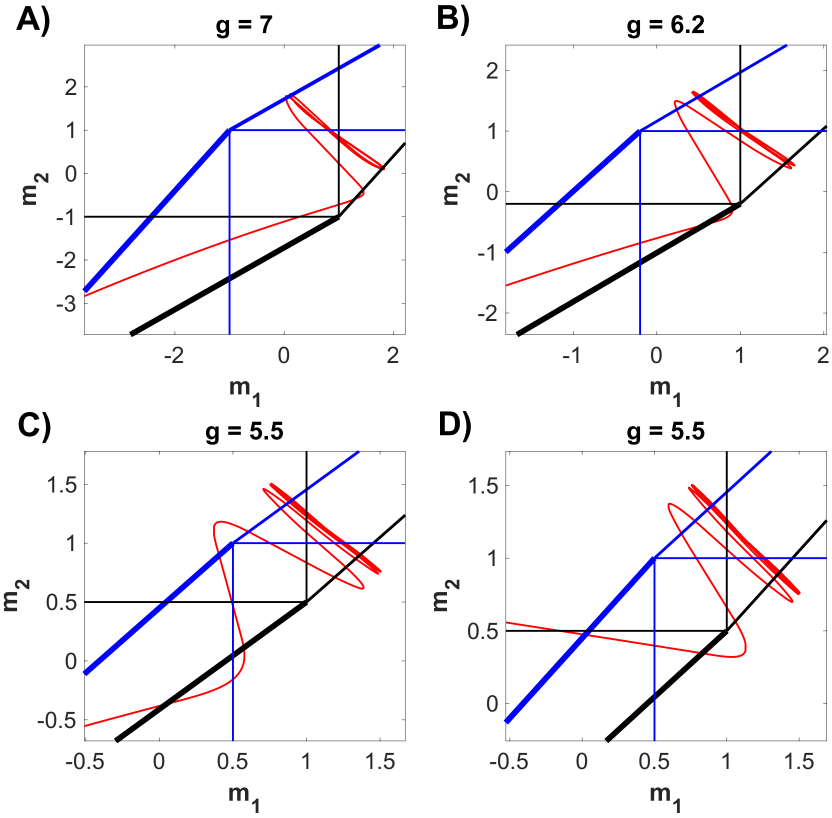

Figure 10. *Projection of full linear model solution onto* (m_1, m_2)*-space. The kite bounded by* $\Sigma_1, \Sigma_2, \Sigma_3, \Sigma_4$ *is shown in the middle of each figure. Black thick line is* Σ_3 *and blue thick line* Σ_4*. Horizontal/vertical lines are* α, β, $\bar{\alpha}$, *and* $\bar{\beta}$*. Projection of full model solution is shown in red.* (A) $g = 7$, (B) $g = 6.2$, (C) $g = 5.5$, *and* (D) $g = 5.5$ *again, with a different initial condition than in* (C).

Downloaded 09/04/22 to 130.49.198.139 . Redistribution subject to SIAM license or copyright; see https://epubs.siam.org/terms-privacy

Σ_3. After this, it passes from $\bar{Q}$ into $\bar{P}$ and leaves through Σ_1. In all cases, all subsequent exits occur through Σ_1 and Σ_2, as claimed.

Before closing this section, we summarize how we used fast-slow decomposition to analyze periodic solutions of system (3.1). As in the standard fast-slow analysis, we considered slow variables as parameters, identified critical points of the fast subsystem parameterized by these slow variables, and then derived the bifurcation conditions for the fast subsystem in terms of the slow variables. The trajectory of the full system quickly approaches a stable fixed point of the fast subsystem and then stays near the fixed point. During the latter relaxation time period, the slow variables evolve to approach their own fixed point, which depends on the values of the fast variables at the fast subsystem fixed point. Once the trajectory of the slow dynamics hits one of the transition surfaces, the fixed point of the fast subsystem is lost and the trajectory of the whole system jumps to the neighborhood of another fixed point of the fast subsystem. These steps comprise one half-cycle of the periodic solution. In the two-neuron network, the mechanism underlying the periodic solution could thus be explained clearly using fast-slow analysis. In a three-neuron network, however, we shall see that slow dynamics continues to play a role even after the occurrence of a fast subsystem bifurcation that might be expected to initiate a fast transition.

3.2. Three-neuron network.

Now consider the following system that describes the dynamics of three neurons,

$$\begin{aligned} \dot{v}_i &= I - v_i - m_i - g(f(v_{i+1}) + g_r f(v_{i+2})), \\ \dot{m}_i &= \epsilon(v_i - a m_i), \end{aligned} \tag{3.7}$$

where $i \in \{1, 2, 3\}$ and indices are in cyclic order; for example, $f(v_4) := f(v_1)$ and $f(v_5) := f(v_2)$ in the governing equation of v_3. The network architecture is circular, symmetric, and mutually inhibitory. Here, g is again our main bifurcation parameter and we fix $g_r = 1.2$ to introduce the difference in the strengths of inhibition between the two directions around the ring (i.e., the "downhill" and "uphill" directions), as encoded in the differences in the b_{ij} values for different i, j in system (2.2). Other parameter values are the same as in the two-neuron linear system.

3.2.1. Critical points and bifurcation diagram of the system.

We begin by considering existence and stability of critical points for system (3.7). Let (v_1, v_2, v_3) be a critical point and suppose that we obtain $\{x, y, z\}$ after sorting the coordinates of this critical point in decreasing order. Then, we say that this critical point is $(+, I, -)$-type if $x > v_{\max}$, $y \in (v_{\min}, v_{\max})$, and $z < v_{\min}$. Other types of critical points such as $(I, -, -)$-type are defined similarly. First, consider $(-, -, -)$-type critical points. In this case, system (3.7) reduces to

$$\begin{aligned} \dot{v}_i &= I - v_i - m_i, \\ \dot{m}_i &= \epsilon(v_i - a m_i), \end{aligned} \tag{3.8}$$

and we have $v_1 = v_2 = v_3 = I/(1 + 1/a)$ and $m_1 = m_2 = m_3 = I/(1 + a)$ due to symmetry. But $I/(1 + 1/a) > 0$ contradicts the assumption that all $v_i < v_{\min} = 0$, and hence system (3.7) does not have any $(-, -, -)$-type critical points.

Copyright © by SIAM. Unauthorized reproduction of this article is prohibited.

Downloaded 09/04/22 to 130.49.198.139 . Redistribution subject to SIAM license or copyright; see https://epubs.siam.org/terms-privacy

Moving on, we establish the following result regarding the existence and stability of $(I,-,-)$-type critical points.

Proposition 3.3. *The system* (3.7) *has three stable* $(I,-,-)$*-type critical points for* $g > 7.5$.

Proof. Without loss of generality, we consider a fixed point (v_1, v_2, v_3) with $v_1 \in (0, v_{\max})$ and $v_2, v_3 < 0$. System (3.7) then becomes

$$\begin{aligned} \dot{v}_1 &= I - v_1 - m_1, \\ \dot{v}_2 &= I - v_2 - m_2 - gg_r f(v_1), \\ \dot{v}_3 &= I - v_3 - m_3 - gf(v_1), \\ \dot{m}_i &= \epsilon(v_i - am_i), \end{aligned} \tag{3.9}$$

and we obtain

$$(v_1, v_2, v_3) = \left(\frac{aI}{1+a}, \quad \frac{aI}{1+a}\left(1 - \frac{agg_r}{v_{\max}(1+a)}\right), \quad \frac{aI}{1+a}\left(1 - \frac{ag}{v_{\max}(1+a)}\right)\right).$$

From the assumption that $v_1 \in (0, v_{\max})$ and $v_2, v_3 < 0$, we find that

$$g > v_{\max}\left(\frac{a+1}{a}\right) = 7.5.$$

To determine the stability of this critical point, we linearize the system of equations (3.7) and obtain a 6×6 matrix, and by direct calculation we confirm that this matrix has two negative eigenvalues, each of multiplicity three. ■

Similarly, for the existence and stability of $(I, I, -)$-type critical points, we have the following result.

Proposition 3.4. *The system* (3.7) *has three unstable* $(I, I, -)$*-type critical points for* $g > 7.5$.

Proof. Without loss of generality, we consider a fixed point (v_1, v_2, v_3) with $v_1, v_2 \in (0, v_{\max})$ and $v_3 < 0$. System (3.7) then becomes

$$\begin{aligned} \dot{v}_1 &= I - v_1 - m_1 - gf(v_2), \\ \dot{v}_2 &= I - v_2 - m_2 - g\, g_r f(v_1), \\ \dot{v}_3 &= I - v_3 - m_3 - g(f(v_1) + g_r f(v_2)), \\ \dot{m}_i &= \epsilon(v_i - am_i). \end{aligned} \tag{3.10}$$

From the first and second equations of (3.10), we have

$$\begin{pmatrix} v_1 \\ v_2 \end{pmatrix} = \frac{I}{(a+1)^2/a^2 - G_1 G_2} \begin{pmatrix} (a+1)/a - G_1 \\ (a+1)/a - G_2 \end{pmatrix}, \tag{3.11}$$

Copyright © by SIAM. Unauthorized reproduction of this article is prohibited.

Downloaded 09/04/22 to 130.49.198.139 . Redistribution subject to SIAM license or copyright; see https://epubs.siam.org/terms-privacy

where $G_1 = g/(v_{\max} - v_{\min})$ and $G_2 = g_r G_1$. Putting these two equations into the third equation of (3.10), we obtain

$$v_3 = \frac{a}{a+1}\left[I - \frac{gI}{v_{\max}\left((a+1)^2/a^2 - G_1G_2\right)}\left\{(1+g_r)\frac{a+1}{a} - \frac{g}{v_{\max}}\left(1+g_r^2\right)\right\}\right]. \tag{3.12}$$

Now, the condition $v_1 \in (0, v_{\max})$ yields

$$-\frac{v_{\max}}{\sqrt{g_r}}\frac{a+1}{a} < g < \frac{v_{\max}}{\sqrt{g_r}}\frac{a+1}{a} \qquad \text{or} \qquad g > v_{\max}\frac{a+1}{a} \tag{3.13}$$

and the condition $v_2 \in (0, v_{\max})$ yields

$$-\frac{v_{\max}}{\sqrt{g_r}}\frac{a+1}{a} < g < \frac{v_{\max}}{g_r}\frac{a+1}{a} \qquad \text{or} \qquad g > \frac{v_{\max}}{\sqrt{g_r}}\frac{a+1}{a}. \tag{3.14}$$

From the condition that $v_3 < 0$, we also have

$$\frac{\left(g_r^2 - g_r + 1\right)g^2 - v_{\max}(1+g_r)(a+1)/a\, g + v_{\max}^2(a+1)^2/a^2}{v_{\max}^2\left((a+1)^2/a^2 - g_r g^2\right)} < 0.$$

Note that the numerator of this fraction is always positive because $g_r^2 - g_r + 1 > 0$ and

$$\left\{v_{\max}(1+g_r)\frac{a+1}{a}\right\}^2 - 4\left(g_r^2 - g_r + 1\right)v_{\max}^2\left(\frac{a+1}{a}\right)^2 = -3\left(v_{\max}\frac{a+1}{a}\right)^2(g_r - 1)^2 < 0.$$

Thus, the condition that $v_3 < 0$ yields

$$g < -\frac{v_{\max}}{\sqrt{g_r}}\frac{a+1}{a} \qquad \text{or} \qquad g > \frac{v_{\max}}{\sqrt{g_r}}\frac{a+1}{a}. \tag{3.15}$$

Combining (3.13), (3.14), and (3.15), we obtain $g > v_{\max}(a+1)/a = 7.5$. Now, the linearization of the system (3.7) around this fixed point is a 6×6 matrix and the characteristic polynomial of this matrix is given by

$$\begin{aligned}&\left\{\lambda^2 + (a\epsilon + 1)\lambda + \epsilon(a+1)\right\}\left\{\lambda^2 + (a\epsilon + 1 - \sqrt{G_1G_2})\lambda + \epsilon(a + 1 - a\sqrt{G_1G_2})\right\}\\ &\times\left\{\lambda^2 + (a\epsilon + 1 + \sqrt{G_1G_2})\lambda + \epsilon(a + 1 + a\sqrt{G_1G_2})\right\} = 0.\end{aligned}$$

Here we consider the second factor of this characteristic polynomial. We note that $a\epsilon + 1 - \sqrt{G_1G_2} < 0$ and $a + 1 - a\sqrt{G_1G_2} < 0$ for $g > 7.5$. Thus, as a quadratic equation in λ, the second factor of this characteristic polynomial has a positive real root and the critical point is unstable. ■

Copyright © by SIAM. Unauthorized reproduction of this article is prohibited.

Downloaded 09/04/22 to 130.49.198.139 . Redistribution subject to SIAM license or copyright; see https://epubs.siam.org/terms-privacy

Next, consider any $(+,-,-)$-type critical point, say, a critical point (v_1, v_2, v_3) with $v_1 > v_{\max}$ and $v_2, v_3 < 0$. From system (3.7), we obtain

$$(v_1, v_2, v_3) = \left(\frac{aI}{a+1}, \quad \frac{a(I - gg_r)}{a+1}, \quad \frac{a(I-g)}{a+1} \right)$$

but since $aI/(a+1) < v_{\max}$, this point does not satisfy the prescribed condition on v_1, so system (3.7) does not have a $(+,-,-)$-type critical point. Similar analysis also shows that system (3.7) does not have a $(+, I, -)$-type critical point. For example, consider a fixed point with $v_1 > v_{\max}$, $v_2 \in (0, v_{\max})$, and $v_3 < 0$. From system (3.7), we have $v_1 = a/(a+1)(I - gv_2/v_{\max}) > v_{\max}$, which yields $I - (a+1)v_{\max}/a > gv_2/v_{\max}$. Note that the left side of this inequality is negative while the right side is positive and thus it fails. In fact, we can show that system (3.7) does not have critical points of any of the remaining types except (I, I, I)-type. We establish the following result regarding the existence and stability of (I, I, I)-type critical points.

Proposition 3.5. *System (3.7) has an (I, I, I)-type critical point, which is stable for $g < g_{h1} \approx 4.56663$. At $g = g_{h1}$, a pair of complex conjugate eigenvalues cross the imaginary axis in the positive direction and the critical point becomes unstable. At $g = g_{h2} \approx 5.07986$, another pair of complex conjugate eigenvalues also leave the negative real half-plane, and they return at $g = g_{h3} \approx 6.16515$.*

Proof. Due to symmetry, system (3.7) has a critical point $(v, v, v, v/a, v/a, v/a)$, where

$$v = \frac{I}{(a+1)/a + g(1+g_r)/v_{\max}} > 0.$$

It is also easily shown that $v < v_{\max}$ for $g > 0$. To determine the stability of this critical point we linearize system (3.7) and obtain a 6×6 matrix with characteristic polynomial given by

$$\begin{aligned} &(\Lambda\Gamma + \epsilon + \quad G_1\Lambda + G_2\Lambda) \\ &\times\{(\Lambda\Gamma + \quad \epsilon)^2 + (G_1\Lambda)^2 + (G_2\Lambda)^2 - (\Lambda\Gamma + \epsilon)G_1\Lambda - (\Lambda\Gamma + \epsilon)G_2\Lambda - G_1G_2\Lambda^2\} = 0, \end{aligned}$$

where $\Lambda = a\epsilon + \lambda$ and $\Gamma = 1 + \lambda$. From the first factor of this equation, we have

$$(a\epsilon + \lambda)(1+\lambda) + \epsilon + (G_1 + G_2)(a\epsilon + \lambda) = 0, \tag{3.16}$$

which yields

$$\lambda_{1,2} = \frac{-(1 + a\epsilon + G_1 + G_2) \pm \sqrt{(1 + a\epsilon + G_1 + G_2)^2 - 4\epsilon(a + 1 + (G_1 + G_2)a)}}{2}.$$

The quantity inside the square root can be written as

$$(1 + a\epsilon + G_1 + G_2)^2 - 4\epsilon(a + 1 + (G_1 + G_2)a) = (G_1 + G_2 + 1 - a\epsilon)^2 - 4\epsilon > 0.$$

Therefore, $\lambda_{1,2}$ are negative real numbers.

Copyright © by SIAM. Unauthorized reproduction of this article is prohibited.

Downloaded 09/04/22 to 130.49.198.139 . Redistribution subject to SIAM license or copyright; see https://epubs.siam.org/terms-privacy

Now, using the fact that $\Gamma = \Lambda - a\epsilon + 1$ or $\Lambda\Gamma = \Lambda^2 + (1 - a\epsilon)\Lambda$, the second factor of the characteristic polynomial can be written as

$$\begin{aligned} 0 &= (\Lambda^2 + (1 - a\epsilon)\Lambda + \epsilon)^2 + (G_1^2 + G_2^2)\Lambda^2 - (\Lambda^2 + (1 - a\epsilon)\Lambda + \epsilon)(G_1 + G_2)\Lambda - G_1G_2\Lambda^2 \\ &= \left\{\Lambda^2 + (1 - a\epsilon)\Lambda + \epsilon - \frac{1}{2}(G_1 + G_2)\Lambda\right\}^2 + \frac{3}{4}\{(G_2 - G_1)\Lambda\}^2 . \end{aligned}$$

Therefore,

$$\Lambda^2 + (1 - a\epsilon)\Lambda + \epsilon - \frac{1}{2}(G_1 + G_2)\Lambda = \pm i\frac{\sqrt{3}}{2}(G_2 - G_1)\Lambda.$$

If we let $\Phi = 1 - a\epsilon - (G_1 + G_2)/2$ and $\Psi = \sqrt{3}(G_2 - G_1)/2$, then this equation becomes $\Lambda^2 + \Phi\Lambda + \epsilon = i\Psi\Lambda$, and if we also let $\Lambda = R + iI$ where $R, I \in \mathbb{R}$, then we obtain the following system of equations:

$$\begin{cases} R^2 - I^2 + \Phi R + \epsilon = -\Psi I, \\ 2RI + \Phi I = \Psi R. \end{cases}$$

Now, the first of these equations can be written as

$$(R + \Phi/2)^2 - (I - \Psi/2)^2 = (\Phi/2)^2 - (\Psi/2)^2 - \epsilon, \tag{3.17}$$

which is a hyperbola unless $(\Phi/2)^2 - (\Psi/2)^2 - \epsilon = 0$. The second equation also can be written as

$$I = \Psi/2 - \frac{\Psi\Phi/4}{R + \Phi/2}, \tag{3.18}$$

which is another hyperbola unless $\Phi = 0$. To find an explicit formula for $\bar{R} := Re(\lambda) = Re(\Lambda - a\epsilon) = R - a\epsilon$, we let $X = (R + \Phi/2)^2 > 0$. Then, (3.17) and (3.18) give us

$$X - \frac{(\Psi\Phi/4)^2}{X} = (\Phi/2)^2 - (\Psi/2)^2 - \epsilon.$$

Solving this equation for X and then expressing the result in terms of $\bar{R}$, we have

$$\bar{R} = -a\epsilon - \frac{\Phi}{2} \pm \sqrt{\frac{(\Phi/2)^2 - (\Psi/2)^2 - \epsilon + \sqrt{((\Phi/2)^2 - (\Psi/2)^2 - \epsilon)^2 + (\Psi\Phi)^2/4}}{2}}. \tag{3.19}$$

The plus branch of (3.19) is negative when $\Phi = \Psi$, is monotone increasing over the g values where $\Phi > \Psi$, and, for our parameter values, has a unique root at $g = g_{h1} :\approx 4.5666$. Meanwhile, we can calculate that the minus branch of (3.19) is also negative when $\Phi = \Psi$ as well as in the limit as $g \to \infty$, and substituting our parameter values into (3.19) shows that it has roots at $g = g_{h2} :\approx 5.0798, g_{h3} :\approx 6.16515$, as desired. ■

Before moving on, we illustrate these results numerically. Figure 11 shows two curves, one defined by (3.17) (red) and one by (3.18) (blue), in the (Re(λ),Im(λ)) or equivalently the $(\bar{R}, I)$ plane when $g = 4.5$ (Figure 11(A)) and $g = 4.6$ (Figure 11(B)). When $g = 4.5$, there

Copyright © by SIAM. Unauthorized reproduction of this article is prohibited.

Downloaded 09/04/22 to 130.49.198.139 . Redistribution subject to SIAM license or copyright; see https://epubs.siam.org/terms-privacy

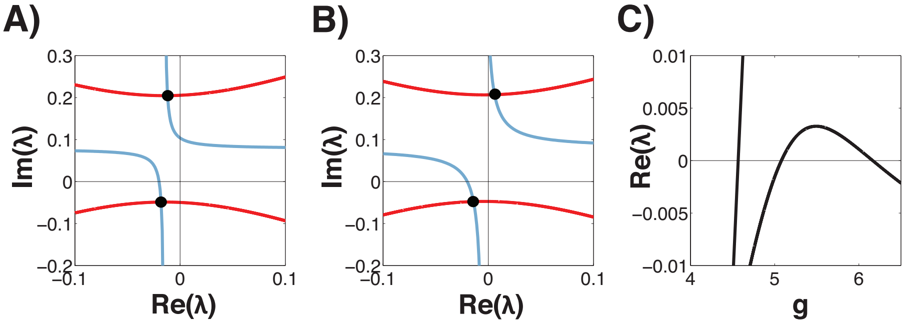

Figure 11. *Solutions of* (3.17) *(red) and* (3.18) *(blue) in the (*Re*(*λ*),*Im*(*λ*)) plane.* (A), (B) *Solution curves and their intersections (black dots) for* $g = 4.5$ (A) *and* 4.6 (B). (C) *Real parts of complex eigenvalues (*Re*(*λ*)* $= \bar{R}$*) as parameter g varies. At* $g \approx 4.5666$*, two eigenvalues cross the imaginary axis to have positive real part, and at* $g \approx 5.0798$*, the remaining two eigenvalues also cross the imaginary axis. Note that at* $g = 49/11$*,* $\Phi = 0$*.*

are two intersection points with negative $\mathrm{Re}(\lambda)$ values, which means there are four complex eigenvalues with negative real parts. As g increases, the vertical asymptote $\bar{R} = -a\epsilon - \Phi/2$ of (3.18) moves rightward and so do the two intersection points. At $g = g_{h1} :\approx 4.5666$, a pair of complex conjugate eigenvalues cross the imaginary axis to have positive real parts (Figure 11(C)). Thus, the critical point loses stability. Figure 11(B) shows that the upper intersection point has already crossed the imaginary axis when $g = 4.6$. Figure 11(C) also shows that the other intersection point, hence the other pair of complex conjugate eigenvalues, also moves through the imaginary axis from the negative to the positive real half-plane at $g = g_{h2} :\approx 5.0798$ and returns back to the negative real half-plane at $g = g_{h3} :\approx 6.16515$.

Using XPPAUT, we computed a bifurcation diagram for system (3.7) with respect to parameter g, which shows that g_{h1}, g_{h2}, and g_{h3} correspond to Andronov–Hopf (HB) bifurcation points (Figure 12). The middle solid curve that cuts through the diagram horizontally consists of (I, I, I)-type fixed points. The set of stable fixed points among them is denoted by a thick curve and unstable fixed points by a thin curve. There are three HB bifurcation points at $g = g_{h1}$, g_{h2}, and g_{h_3}. As g passes through g_{h1}, the stable fixed points lose stability and a branch of periodic orbits emerges; these start out unstable (green) but give way to a branch of stable periodic orbits (blue) almost immediately, presubmably through a saddle-node of periodic orbits bifurcation (Figure 12(A)). These stable periodic solutions are SOs. At another HB point, $g = g_{h2}$, a branch of unstable periodic orbits emanates, which terminates at $g = g_{h3}$. The minimum and maximum values of v_1 are denoted by green dots, which form a closed curve surrounding part of the fixed point branch in the middle of Figure 12(A).

Now, as g increases, the stable branch of SOs gives rise to two unstable branches of periodic orbits (red in Figure 12(B)) at a PD bifurcation point at $g = g_{pd1} :\approx 5.064$. One of these in turn gives rise to a new branch of stable periodic solutions at a second PD bifurcation at $g = g_{pd2} :\approx 5.375$ (also solid blue in Figure 12(A)–(B), labeled with **D**). These stable periodic solutions are DROs. The other branch of unstable periodic solutions born at $g = g_{pd1}$ extends in the direction $g < g_{pd1}$ until it turns around at $g = g_{pd3} \approx 4.994$ and becomes a third branch of stable periodic solutions (solid black in Figures 12(A)–(B), labeled with **U**). These stable periodic solutions are UROs. This stable branch of relaxation oscillations meets the

Copyright © by SIAM. Unauthorized reproduction of this article is prohibited.

Downloaded 09/04/22 to 130.49.198.139 . Redistribution subject to SIAM license or copyright; see https://epubs.siam.org/terms-privacy

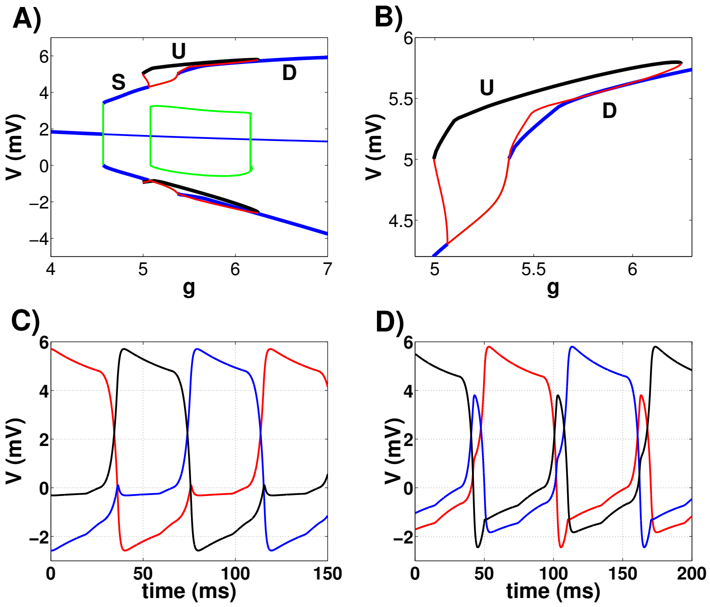

Figure 12. (A) *Numerically computed bifurcation diagram of the system* (3.7) *with bifurcation parameter* g. (B) *Upper middle branches are zoomed in.* (C) *DROs when* $g = 6.2$. (D) *UROs when* $g = 6.2$

other branch of unstable periodic solutions at $g = g_{pd4} \approx 6.245$. As illustrated in Figure 12(B), there is a small range of g values near 5 over which UROs and SOs stably co-exist and a large range of g values over which UROs and DROs stably co-exist (Figure 12(B)). All of these features agree qualitatively with the bifurcation diagram in Figure 2 from the full model (2.1)–(2.2). In particular, note that the family S grows abruptly in amplitude, as in Figure 2(A), where the piecewise smooth coupling was also used, and that the bifurcations that destabilize and connect the solution branches agree with those in Figure 2(C), which provides additional evidence that these bifurcation types likely occur in Figure 2(A) as well.

Not surprisingly, the activity patterns of SOs, UROs, and DROs are qualitatively the same as those shown in Figure 1. The time courses of DROs and UROs are illustrated in Figures 12(C)–(D). As in Figure 1, SOs and DROs share the same order of activation that can be naturally deduced from the network architecture. In UROs, however, this natural order is reversed.

To make things more clear in the following subsections, we next define some terms related to the fast subsystem. When a neuron is active, we assume that at least one of the inhibited neurons is totally suppressed. More precisely, again taking indices to be cyclic, if v_i is active, then we assume that v_{i+1} is totally suppressed (below $v_{\min}$) all the time except during the transition between states. v_{i-1} (or equivalently v_{i+2}), on the other hand, is near $v_{\min}$ and can potentially be positive. Thus, if v_i is active, then we only need to consider the v_i-nullcline and the v_{i+2}-nullcline to describe the dynamics of the trajectory in the fast subsystem. Consider (v_i, v_{i+2})-space, where the horizontal axis is v_i and vertical axis v_{i+2}. Similarly to the two-neuron network (Figures 6 and 7), over most of the time that v_i is active, the fast subsystem

Copyright © by SIAM. Unauthorized reproduction of this article is prohibited.

Downloaded 09/04/22 to 130.49.198.139 . Redistribution subject to SIAM license or copyright; see https://epubs.siam.org/terms-privacy

has two stable fixed points and one unstable fixed point. The stable fixed point that the projected trajectory approaches is located at the lower right part of (v_i, v_{i+2}) space where v_i is near $v_{\max}$ and v_{i+2} is near $v_{\min}$. At the other stable fixed point, v_i is near $v_{\min}$ and v_{i+2} is near $v_{\max}$. We call the former the *lower fixed point in* (v_i, v_{i+2}) *space* and denote it by FP_L in (v_i, v_{i+2}) space. Similarly, we call the latter the *upper fixed point in* (v_i, v_{i+2}) *space* and denote it by FP_U in (v_i, v_{i+2}) space. Note that we will use these labels regardless of which i value we are considering; the specific fixed points to which they refer when used below will be clear from the context. Finally, at the unstable fixed point, v_i and v_{i+2} take intermediate values between $v_{\min}$ and $v_{\max}$.

3.2.2. Adaptive release and adaptive escape mechanisms. Before we study some important features of DRO and URO activity patterns in more detail, we first consider how the transition between states is initiated. As a concrete example, we consider the transition from the v_1-on state to the v_3-on state in DROs. We show that there are two different transition mechanisms depending on the synaptic strength (the value of parameter g), which also carry over to UROs. In the following subsections, we study what happens in the transitions of UROs and DROs by considering fast subsystems during fast jumps. This will reveal the mechanism that determines, via the interplay between slow dynamics and fast dynamics, whether UROs or DROs occur.

Figure 13 shows two relaxation-type oscillations in DROs for $g = 5.6$ (A) and $g = 6.2$ (C). As stated in the previous section, the order of activation in DROs follows the natural order in relation to the current network architecture, that is, $v_1 \to v_3 \to v_2$. With the stronger synaptic strength (Figure 13(C)), an active neuron exerts more inhibition onto the other neurons and we observe that the active neuron stays in its active phase longer and the inhibited neurons are more suppressed. Specifically, when v_1 is active (red traces in both Figures 13(A) and 13(C)), the less inhibited neuron v_3 (black) is below $v_{\min} = 0$ (that is, v_3 is totally suppressed) when $g = 6.2$ (Figures 13(C) and 12(C)) but above $v_{\min}$ over most of the active duration of v_1 when $g = 5.6$.

These different statuses of the less inhibited neuron result in different fast subsystem bifurcation mechanisms between the two examples. The difference between these two mechanisms can be seen more clearly if we look at the fast subspace. Figures 13(B) and 13(D) show the corresponding fast subspace with the v_1 nullcline (black) and v_3 nullcline (blue) when the transition is initiated. At this moment, the stable fixed point and unstable fixed point (intersection points of v_1 nullcline and v_3 nullcline) merge and disappear through a saddle-node bifurcation. In each figure, red dots denote the projection of the trajectory of the whole system just before the transition is initiated. Note that when $g = 5.6$, the saddle-node bifurcation happens at a point on S_3, with the transition between states initiated when the active neuron first decays below $v_{\max}$; when that occurs, the suppressed neuron is already above $v_{\min}$. When $g = 6.2$, on the other hand, the fast subsystem bifurcation happens at a point on S_2 when the suppressed neuron crosses $v_{\min}$, with the active neuron already below $v_{\max}$.

Traditional *release* and *escape* mechanisms [48, 43] are not so well-defined for this system. The case with $g = 5.6$ might be interpreted as a *release* mechanism, because it is only when the active neuron v_1 drops below $v_{\max}$ that the transition can occur, while the case with $g = 6.2$ can be interpreted as an *escape* mechanism, since the transition occurs when v_3 reaches $v_{\min}$.

Downloaded 09/04/22 to 130.49.198.139 . Redistribution subject to SIAM license or copyright; see https://epubs.siam.org/terms-privacy

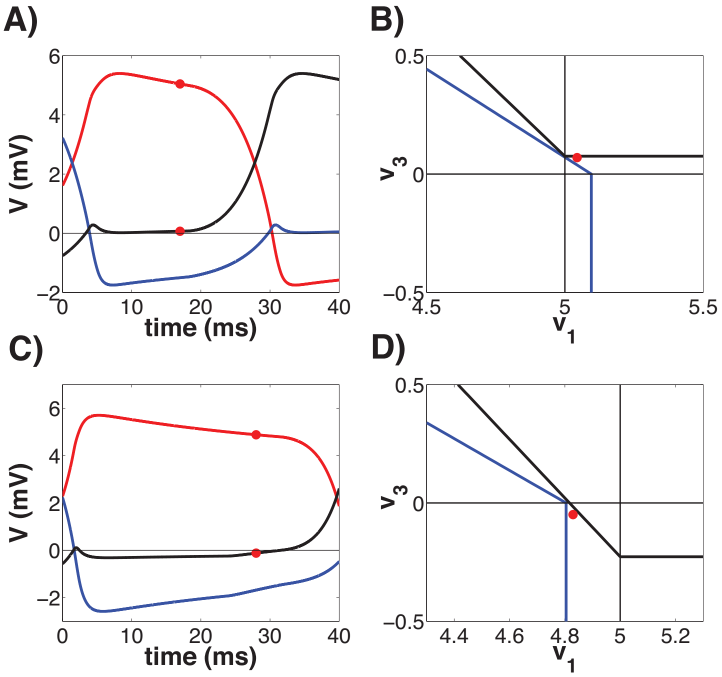

Figure 13. *Two examples of transitions arising for DROs. Adaptive escape example* (A)–(B) *when* $g = 5.6$ *and adaptive release example* (C)–(D) *when* $g = 6.2$*. In* (A) *and* (C)*,* v_1 *is in red,* v_2 *in blue, and* v_3 *in black.* (B) *and* (D) *show the corresponding fast subspace with the* v_1*-nullcline (black) and the* v_3*-nullcline (blue). In each figure, red dots denote the values of* v_1 *and* v_3 *when bifurcation happens, hence the transition is initiated.*

Under the weaker inhibition level, however, we can also argue that we have *escape* because the growth of v_3 above $v_{\min}$ happens first and eventually helps to pull v_1 down. Similarly, under stronger inhibition, we can argue that we have *release* because the reduction in v_1 below $v_{\max}$ is essential for allowing v_3 to grow. While these two interpretations both seem reasonable, we refer to the weak inhibition case as a form of escape and the strong inhibition scenario as a form of release, and the rationale for this choice will be clear in the later part of this section.

Sekerli and Butera refined the escape (E)/release (R) classification into intrinsic E, intrinsic R, synaptic E, and synaptic R [42]. In the first two, the switch mechanism is the usual jump from a knee; that is, the switch from slow to fast flow happens at a saddle-node bifurcation of the fast subsystem. In the synaptic cases, the switch is triggered by a crossing of a synaptic threshold within the slow flow, which can be thought of as causing a jump in the nullclines by fast threshold modulation [46]. In our case, for a model system with voltage-sensitive, piecewise smooth coupling, we first have a synaptic threshold crossing, where a voltage crosses either $v_{\max}$ or $v_{\min}$, but this does not give a discontinuity in the associated synaptic variable nor an immediate fast subsystem bifurcation. Thus, these two mechanisms do not match the Sekerli and Butera scenarios. In fact, these transitions are qualitatively equivalent to the situation dubbed as adaptation by Daun, Rubin, and Rybak [9] in the sense that (1) there is no threshold where the synaptic variable jumps and (2) the lead-up to the transition between states involves a gradual change in the inhibitory synaptic strength from one of the two transitioning

Copyright © by SIAM. Unauthorized reproduction of this article is prohibited.

cells to the other. For this reason, we call the transition with $g = 5.6$ *adaptive escape* and that with $g = 6.2$ *adaptive release*. Note that in the two-neuron network, *adaptive release* is the only transition mechanism that occurs, at least after an initial transient (Figures 8 and 10).

As in the case of the two-neuron network (refer to Figure 6 and related paragraphs and equations), we can derive the equations of the transition surfaces Σ_2 and Σ_3 in the three-neuron network. We still assume that when a neuron is active, at least one of the inhibited neurons is totally suppressed over the active period; that is, the more inhibited neuron never rises above $v_{\min}$ between transitions. As a concrete example, we consider the transition from the v_1-on state to the v_3-on state. When v_1 is active, v_2 is totally suppressed over the active period of v_1 by assumption and system (3.7) is reduced to

$$\begin{aligned} \dot{v}_1 &= I - v_1 - m_1 - gg_r f(v_3), \\ \dot{v}_2 &= I - v_2 - m_2 - g(f(v_3) + g_r f(v_1)), \\ \dot{v}_3 &= I - v_3 - m_3 - gf(v_1). \end{aligned} \tag{3.20}$$

System (3.20) demonstrates that activity patterns in the v_1-on state can be described by the dynamics of v_1 and v_3 only; that is, this dynamics is not influenced by v_2. Thus, we only need to consider the v_1- and v_3-nullclines in (v_1, v_3)-space to derive the equations of the transition surfaces. Recall that the transition from the v_1-on to the v_3-on state can happen only on the line segments $S_2\,(v_{\min} < v_1 < v_{\max},\ v_3 = v_{\min})$ and $S_3\,(v_{\min} < v_3 < v_{\max},\ v_1 = v_{\max})$ in (v_1, v_3)-space (Figure 6). Note that a fast subsystem bifurcation on S_2 corresponds to *adaptive release* and on S_3 to *adaptive escape*. Now, for the transition to happen on the line segment S_2 in (v_1, v_3) space, the right elbow of the v_1-nullcline, $(I - m_1, 0)$, should lie on the line segment S_2 and on the middle branch of v_3-nullcline, $v_3 = I - m_3 - gv_1/v_{\max}$, at the same time. From the S_2 condition, we find that $I - v_{\max} < m_1 < I$ and, when we also include the v_3-nullcline condition, we obtain

$$m_3 = I - \frac{g}{v_{\max}}(I - m_1).$$

Hence, the transition surface for *adaptive release* is given by

$$\Sigma_2 : \quad I - v_{\max} < m_1 < I \quad \text{and} \quad m_3 = I - \frac{g}{v_{\max}}(I - m_1). \tag{3.21}$$

Similarly, the transition surface for *adaptive escape* is given by

$$\Sigma_3 : \quad I - v_{\max} - gg_r < m_1 < I - v_{\max} \quad \text{and} \quad m_3 = I - g + \frac{v_{\max}}{gg_r}(m_1 - I + v_{\max}). \tag{3.22}$$

These two surfaces act as transition surfaces for the termination of the v_1-on state in (m_1, m_3)-space. (Similarly, we can define transition surfaces to leave the v_2-on state and the v_3-on state.) If the projection of the trajectory of the full system onto (m_1, m_3) hits one of these two surfaces, then a saddle-node bifurcation of the fast subsystem happens and a transition from the v_1-on state to the v_3-on state is initiated. Now, Figure 14 shows the projection of these transition surfaces onto (m_1, m_3)-space along with the projection of the solution of

Downloaded 09/04/22 to 130.49.198.139 . Redistribution subject to SIAM license or copyright; see https://epubs.siam.org/terms-privacy

Copyright © by SIAM. Unauthorized reproduction of this article is prohibited.

Downloaded 09/04/22 to 130.49.198.139 . Redistribution subject to SIAM license or copyright; see https://epubs.siam.org/terms-privacy

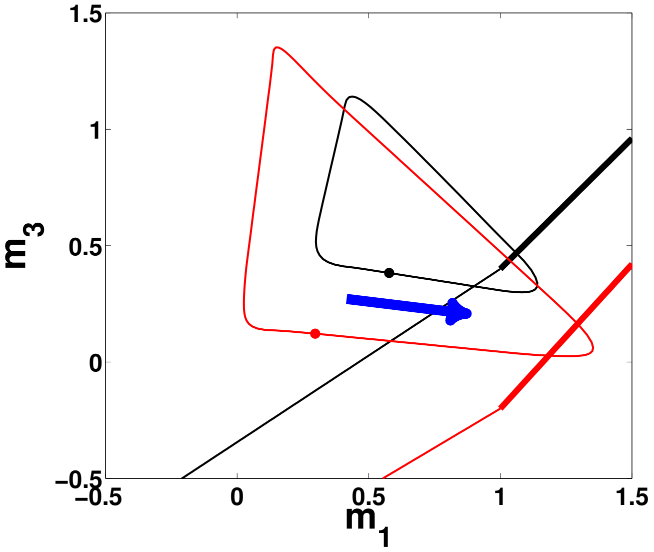

Figure 14. *Projection of transition surfaces (piecewise-linear curves) onto (m_1, m_3)-space along with the projection of trajectories of the full linear system (triangular closed loops) for $g = 5.6$ (black) and $g = 6.2$ (red). In each case, the dot denotes the moment when v_1 assumes its maximum, and the trajectory evolves counterclockwise. The trajectory hits the transition surface for adaptive escape (Σ_3, thin black curve) when $g = 5.6$ and the transition surface for adaptive release (Σ_2, thick red curve) when $g = 6.2$.*

the full system (triangular closed loops) for $g = 5.6$ (black) and $g = 6.2$ (red). The projected transition surface for each case is composed of two pieces, Σ_2 (thick curve) and Σ_3 (thin curve). For clarity, we denote the moment when v_1 assumes its maximum over its active period by a dot in the figure. Over the active period of v_1, m_1 increases and m_3 decreases, and thus the projection of the trajectory of the full system rotates counterclockwise over time and finally hits one of the transition surfaces. When $g = 5.6$, the projection of the trajectory hits Σ_3 (*adaptive escape*), and when $g = 6.2$, the projection of the trajectory hits Σ_2 (*adaptive release*).

Now, we would like to give an analytical argument for why larger g favors the adaptive release mechanism by plotting transition curves in (v, m)-space. We first summarize the conditions for the adaptive escape and adaptive release mechanisms. In the adaptive escape case ($m_1 < I - v_{\max}$),

$$\begin{aligned} m_3 &= I - g + \frac{v_{\max}}{g \cdot g_r}(m_1 - I + v_{\max}), \\ v_1 &= v_{\max}, \text{ and} \\ v_3 &= I - m_3 - g = -\frac{v_{\max}}{g \cdot g_r}(m_1 - I + v_{\max}). \end{aligned} \tag{3.23}$$

In the adaptive release case ($m_1 > I - v_{\max}$),

$$\begin{aligned} m_3 &= I - \frac{g}{v_{\max}}(I - m_1), \\ v_1 &= I - m_1, \text{ and} \\ v_3 &= 0. \end{aligned} \tag{3.24}$$

Copyright © by SIAM. Unauthorized reproduction of this article is prohibited.

Downloaded 09/04/22 to 130.49.198.139 . Redistribution subject to SIAM license or copyright; see https://epubs.siam.org/terms-privacy

In (v_1, m_1)-space, equations (3.23) reduce to

$$v_1 = v_{\max} \quad \text{for} \quad m_1 < I - v_{\max}. \tag{3.25}$$

In (v_3, m_3)-space, equations (3.23) reduce to

$$m_3 = -v_3 + I - g \quad \text{for} \quad v_3 > 0.$$

But, since the fast subsystem bifurcation happens when v_1 decays past $v_{\max}$ in adaptive escape, we only need the first condition, (3.25). Similarly, in (v_3, m_3)-space, equations (3.24) reduce to

$$v_3 = 0 \quad \text{for} \quad m_3 > I - g. \tag{3.26}$$

Here we note that the transition curve for adaptive escape, (3.25), does not depend on g but the adaptive release transition curve, (3.26), does. In fact, the bottom end of the adaptive release transition curve is given by $m_3 = I - g$. Figures 15(B)–(F) and Figures 16(B)–(F) provide a combined view of these transition curves, (3.25), and (3.26), when $g = 5.6$ and $g = 6.2$, respectively; that is, the plots show a (v, m)-space in which we combine (v_1, m_1) and (v_3, m_3) information so that we can track the dynamics of both neurons together. In both figures, the right thick vertical line is the transition curve for the adaptive escape mechanism, (3.25), and the left thick vertical line is the curve for the adaptive release mechanism, (3.26).

Figure 15(A) shows the temporal profiles of v_1 (red) and v_3 (black) and five time points chosen for illustration when $g = 5.6$. Figures 15(B) through 15(F) correspond to the time points in Figure 15(A) in order of occurrence. In Figures 15(B)–(F), the v_1-nullcline (red) and v_3-nullcline (black) are shown along with the projection of the trajectories of neuron 1 (red dot) and neuron 3 (black dot) at each time step. Each blue line is the m-nullcline, which is the same, $m = v/a$, for neuron 1 and neuron 3. The intersection of the v_1-nullcine and the m-nullcline is a fixed point of the (v_1, m_1)-system (not shown in the figure), and hence neuron 1 (red dot) slowly approaches this fixed point along the v_1-nullcline. Similarly, neuron 3 (black dot) slowly approaches a fixed point of the (v_3, m_3)-system along the v_3-nullcline.

Figure 15(B) shows the moment when neuron 3 crosses the line $v_3 = 0$ near the point $(0, I - g)$, the lower end of the adaptive release transition curve. Here we note that if v_1 is fully active ($v_1 > v_{\max}$), then the v_3-nullcline ($m_3 = -v_3 + I - g$) goes through the lower end point of the adaptive release transition curve. Here, the relative m values of the two neurons do not allow for an immediate transition. Once past the line $v_3 = 0$, v_3 becomes positive, which lowers the v_1-nullcline (Figures 15(C)–(F)). Hence the fixed point of the (v_1, m_1)-system moves to the left and downward and the trajectory of neuron 1 adjusts accordingly. Eventually neuron 1 crosses the adaptive escape transition curve (Figures 15(E)–(F)) and a fast subsystem bifurcation occurs. In summary, the characteristic of this mechanism is the lowering of the v_1-nullcline through the growth of v_3 above $v_{\min}$.

When $g = 6.2$, on the other hand, the location of the v_3 fixed point plays a crucial role. Note that the v_3 fixed point is given by $(2(I - g)/3,\ (I - g)/3)$, which is a function of g; if $g < I$, then the fixed point lies in the first quadrant in (v, m)-space, and if $g > I$, then it lies in the third quadrant. Thus, when $g > I$, the passage through $v_3 = 0$ is blocked by the v_3

Copyright © by SIAM. Unauthorized reproduction of this article is prohibited.

Downloaded 09/04/22 to 130.49.198.139 . Redistribution subject to SIAM license or copyright; see https://epubs.siam.org/terms-privacy

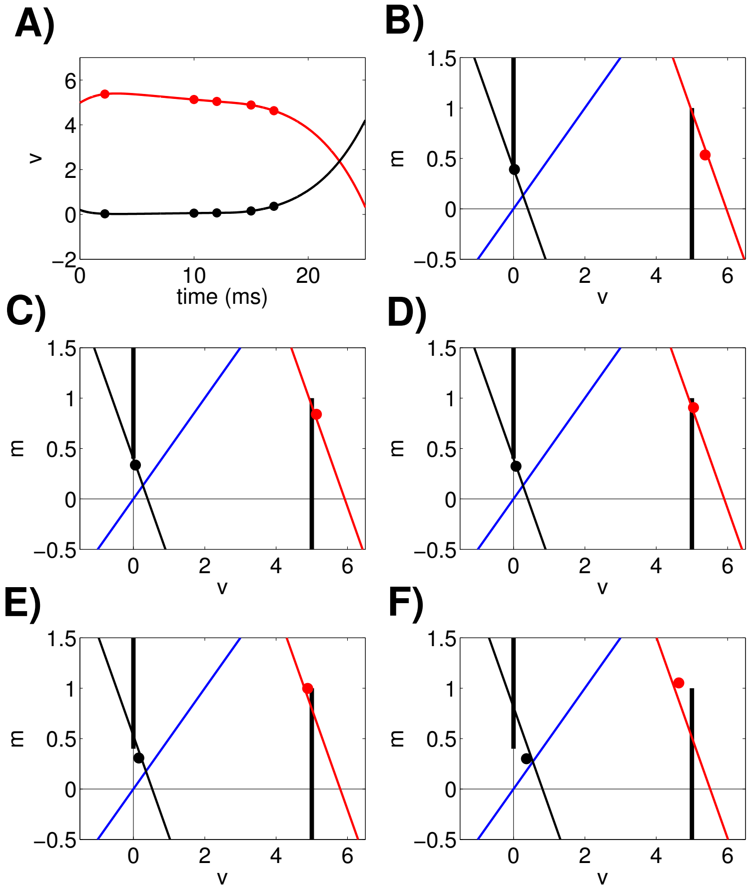

Figure 15. *Adaptive escape in DROs when* $g = 5.6$. (A) *Time courses of* v_1 *and* v_3 *while neuron* 1 *is active. Time points marked with dots are illustrated in the subsequent panels, in order from earliest time to latest time.* (B)–(F) *Snapshots of positions of* (v_1, m_1) *and* (v_3, m_3) *(red and black dots, resp.) plotted in a common* (v, m) *phase plane. Each panel includes the* v_1 *nullcline (thin red), the* v_3 *nullcline (thin black), the* m *nullcline shared by both cells (blue), and the adaptive escape (AE) and release (AR) curves defined by* (3.25), (3.26), *resp. (thick black). In* (B), *note that the bottom point of the AR curve lies on the* v_3 *nullcline and no transition occurs when* v_3 *increases through* $v_{min} = 0$. *In* (D), *the trajectory for cell* 1 *hits the AE curve where it intersects with the* v_1 *nullcline, initiating a transition by adaptive escape.*

fixed point if v_1 is fully active ($v_1 > v_{\max}$) (Figures 16(B)–(C)). If the approach of neuron 1 toward its fixed point carries neuron 1 below $v_1 = v_{\max}$, then the v_3-nullcline is shifted upward accordingly due to the reduced inhibition from v_1 (Figure 16(D)). Hence, neuron 3 is released to eventually cross $v_3 = 0$ through the adaptive release transition curve (Figures 16(E)–(F)). In summary, for $g > I$, adaptive release is the only transition mechanism available, and this observation explains why larger g favors adaptive release.

3.2.3. The loss of downhill relaxation oscillations as g decreases. In this section, we consider the loss of DROs that happens at $g = g_{pd2} :\approx 5.375$ (Figure 12(B)). We look into

Copyright © by SIAM. Unauthorized reproduction of this article is prohibited.

Downloaded 09/04/22 to 130.49.198.139 . Redistribution subject to SIAM license or copyright; see https://epubs.siam.org/terms-privacy

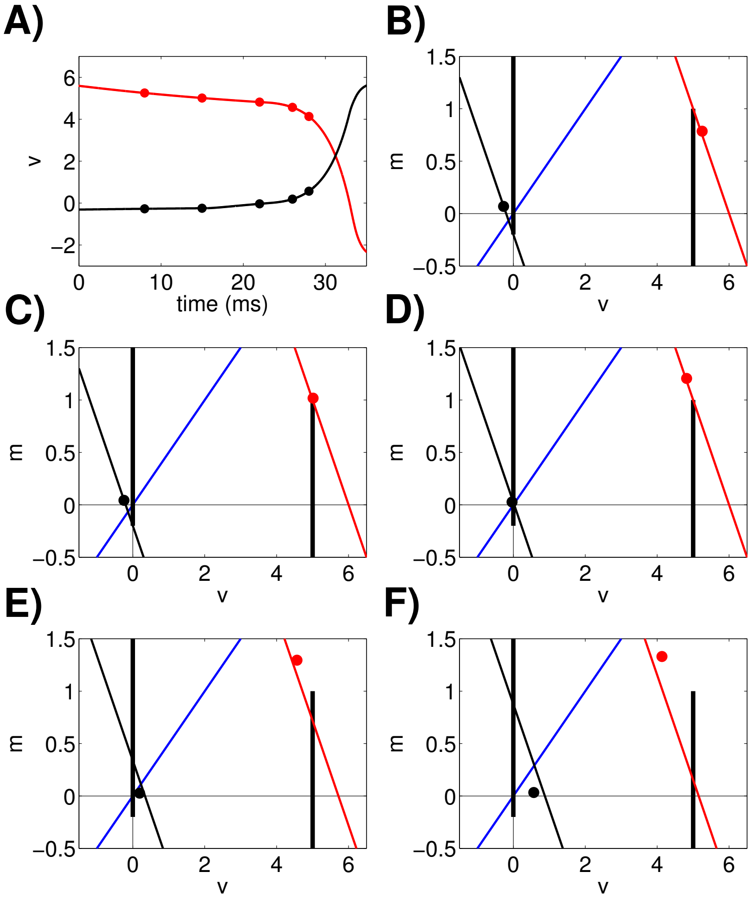

Figure 16. *Adaptive release in DROs when* $g = 6.2$*.* (A) *Time courses of* v_1 *and* v_3 *while neuron* 1 *is active. Time points marked with dots are illustrated in the subsequent panels, in order from earliest time to latest time.* (B)–(F) *Snapshots of positions of* (v_1, m_1) *and* (v_3, m_3) *(red and black dots, resp.) plotted in a common* (v, m) *phase plane. Each panel includes the* v_1 *nullcline (thin red), the* v_3 *nullcline (thin black), the* m *nullcline shared by both cells (blue), and the adaptive escape (AE) and release (AR) curves defined by* (3.25)*,* (3.26)*, resp. (thick black). In* (B)*, note that the top point of the AE curve lies on the* v_1 *nullcline and no transition occurs when* v_1 *decreases through* $v_{max} = 5$*. In* (D)*, the trajectory for cell* 3 *hits the AR curve where it intersects with the* v_3 *nullcline, initiating a transition by adaptive release.*

the transition between states more deeply to investigate what is happening during fast jumps. Simple numerical simulation allows us to gain insight about the mechanisms underlying the loss of DROs as g decreases. This analysis will demonstrate some important ideas about the interplay between slow dynamics and fast dynamics during fast jumps.

We first note that g_{pd2} is slightly greater than 5.375; when $g = 5.375$, UROs are the only solution. If we begin with DROs at $g = 5.38$ and change g to 5.375, then numerical simulation shows that we lose DROs after some transient period due to the failure of the trajectory in reaching the fixed point that it was supposed to reach during a transition. For example, during the fast jump that follows the v_1-on state, the DRO trajectory approaches the fixed

Copyright © by SIAM. Unauthorized reproduction of this article is prohibited.

Downloaded 09/04/22 to 130.49.198.139 . Redistribution subject to SIAM license or copyright; see https://epubs.siam.org/terms-privacy

point FP_L in $(v_3,\ v_2)$-space with $0 < v_2 < v_{max}$ and $v_3 > v_{max}$. On each transient cycle during which the trajectory succeeds in reaching a small neighborhood of FP_L, the order of activation is preserved. But, on some cycle, the trajectory fails to reach this neighborhood and the activation order changes, which can result in the emergence of UROs.

To investigate what causes the failure of trajectory to reach close enough to FP_L to complete a transition, we trace the trajectory of the full system in a piecewise way from the v_1-on state to the v_3-on state. In the v_1-on state, through the slow dynamics, a fast subsystem saddle-node bifurcation occurs (e.g., Figures 13(B), (D)) and the transition from the v_1-on state to the v_3-on state is initiated. While the trajectory of the full system heads toward the remaining fixed point in $(v_1,\ v_3)$-space after the bifurcation, v_1 decreases through $v_{\min} = 0$. Once v_1 is turned off, the scene is changed and the trajectory of the full system lies under the control of the (v_2, v_3) dynamics, while v_1 becomes the totally suppressed neuron. At this moment, there are three fast subsystem fixed points in (v_3, v_2)-space: the stable point FP_L, an unstable point that forms a separatrix, and the second stable fixed point, FP_U, with larger v_2 and smaller v_3. The relationship between the trajectory of the full system and the v_3- and v_2-nullclines determines which one the trajectory approaches (cf. Figure 17(B), which shows FP_L and the unstable fixed point). If the trajectory of the full system succeeds

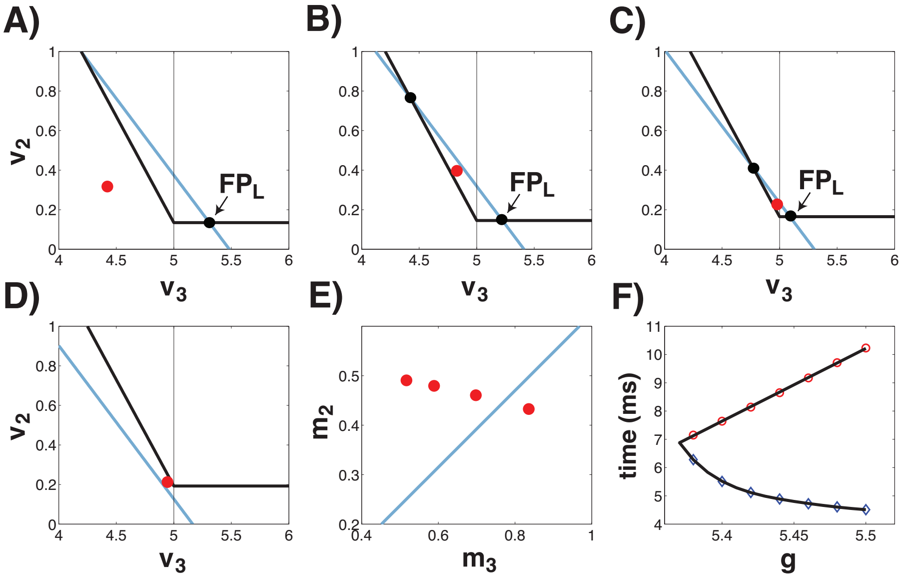

Figure 17. *Transition away from the* v_1*-on state when* $g = 5.375$. (A)–(D) *Four snapshots of the projection of the trajectory of the full system onto* (v_3, v_2)*-space (red dots) along with the* v_3*-nullcline (blue) and the* v_2*-nullcline (black) with* $v_1 < 0$ *in a case where the trajectory does not reach close enough to* FP_L *to complete the transition. Between the two nullclines,* $\dot{v}_2 < 0, \dot{v}_3 > 0$*. Note in panel* (D) *that* FP_L *is gone even though* $v_3 < v_{max}$*.* (E) *Projection of transition surface* Σ_3 *(blue curve) and the trajectory snapshots (red dots), which progress from left to right, into* (m_3, m_2)*-space. When the* (m_3, m_2) *trajectory crosses* Σ_3*, a saddle-node bifurcation of the fast subsystem occurs and* FP_L *is lost.* (F) *Plot of two times, one for the trajectory of the full system to approach* FP_L *(*T_a*, blue diamonds) and the other for the bifurcation that eliminates* FP_L *(*T_b*, red circles), as a function of* g*. Markers denote numerically computed* T_a *and* T_b*. Black curves are curve fittings. For stable DROs (*$g > g_{hd2}$*),* T_a *is substantially smaller than* T_b*, which guarantees the success of the trajectory to approach* FP_L *during the transition.*

Copyright © by SIAM. Unauthorized reproduction of this article is prohibited.

Downloaded 09/04/22 to 130.49.198.139 . Redistribution subject to SIAM license or copyright; see https://epubs.siam.org/terms-privacy

in approaching FP_L, then this completes the transition from the v_1-on state to the v_3-on state. But if the trajectory of the full system fails to reach FP_L before FP_L disappears through a saddle-node bifurcation, then v_3 does not turn on next and the DRO pattern is lost.

What we observe here can be cast as a competition between two times, one for the trajectory of the full system to approach FP_L, say, T_a for approach, and the other for the loss of FP_L to happen, say, T_b for bifurcation, during the transition. We note that T_a is mostly determined by the fast dynamics of (v_2, v_3) and T_b by the slow dynamics of (m_2, m_3). When v_1 shuts off, the projection of the trajectory initially lies in the basin of attraction of FP_L. If T_a is smaller than T_b, then the trajectory converges $O(\epsilon)$-close to the stable FP_L. If T_a is larger than T_b, then FP_L disappears through the saddle-node bifurcation while the projection of the trajectory approaches it and thus the projection of the trajectory turns around and approaches FP_U instead.

Figures 17(A)–(E) display an example in which the trajectory of the full system fails to reach FP_L during the transition away from the v_1-on state. When v_1 turns off, the projection of the trajectory of the full system lies in the basin of attraction for FP_L; that is, it lies in the region to the right of the separatrix that comes from the middle unstable fixed point (Figure 17(A)). While the trajectory approaches the stable FP_L, a saddle-node bifurcation happens and FP_L is lost, and hence the trajectory turns around and heads for FP_U (Figures 17(B)–(D)). Figure 17(E) shows the transition surface Σ_3 (blue line) and the projection of the trajectory (red dots) onto (m_3, m_2) space. The projection of the trajectory moves from left to right over time. When v_1 turns off, (m_3, m_2) lies to the left of Σ_3. As the trajectory of the full system approaches FP_L, (m_3, m_2) hits Σ_3. Thus, a saddle-node bifurcation happens before the trajectory of the full system reaches FP_L. A key point is that even though the approach time T_a is ostensibly measured on the fast timescale and the bifurcation time T_b on the slow timescale, the proximity of the fast nullclines near the bifurcation can cause T_a and T_b to take similar values. Figure 17(F) shows numerically computed T_a (blue diamonds) and T_b (red circles) values as a function of parameter g. As g decreases, the former time increases while the latter decreases. T_a and T_b become quite similar at $g \approx g_{pd2}$.

These results imply that the relevant fast subspace during a transition is transiently partitioned into three subregions and three corresponding activity patterns are possible. In the region to the right of the separatrix that comes out of the unstable fixed point of the fast subsystem, if the trajectory is sufficiently close to FP_L, then the trajectory of the fast subsystem succeeds in equilibrating at FP_L, corresponding to activation of v_3, and then the slow dynamics relaxes to its own fixed point, pulling the slaved, fast variables along the fixed point manifold. If the trajectory lies in the region to the right of the separatrix but is sufficiently close to the separatrix, then while the trajectory of the fast subsystem tries to equilibrate at FP_L, the slow dynamics pushes the fast system through a bifurcation, which forces a second fast jump to a new fixed point manifold, with activation of v_2 and hence a loss of DROs, and then a slow relaxation follows. If the trajectory lies in the region to the left of the separatrix, then the trajectory of the fast subsystem approaches FP_U directly and v_2 activates correspondingly.

Copyright © by SIAM. Unauthorized reproduction of this article is prohibited.

Downloaded 09/04/22 to 130.49.198.139 . Redistribution subject to SIAM license or copyright; see https://epubs.siam.org/terms-privacy

3.2.4. Uphill relaxation oscillations. In this section, we discuss three topics. First, we show that UROs and DROs share the same mechanisms for the initiation of transitions between states. Second, we explain how "turn-around" during fast jumps happens by considering the details of the relevant fast dynamics. Last, we consider how UROs are lost at $g = g_{pd3}$ as g decreases and at g_{pd4} as g increases (Figure 12). In the former case, we find that UROs disappear through the same interaction of fast and slow timescale effects that causes the elimination of DROs.

We begin with an example of UROs when $g = 6.0$ (Figure 18(A)). Unlike in DROs, the voltage traces of the two inhibited neurons follow similar paths in UROs. However, Figure 18(A) suggests that we may still assume that when a neuron is active, one of the inhibited neurons is totally suppressed over the active period. Under this assumption, we can follow the steps from the previous section to derive the equations of the transition surfaces and to conclude that UROs and DROs share the same set of transition surfaces. Figure 18(B) shows

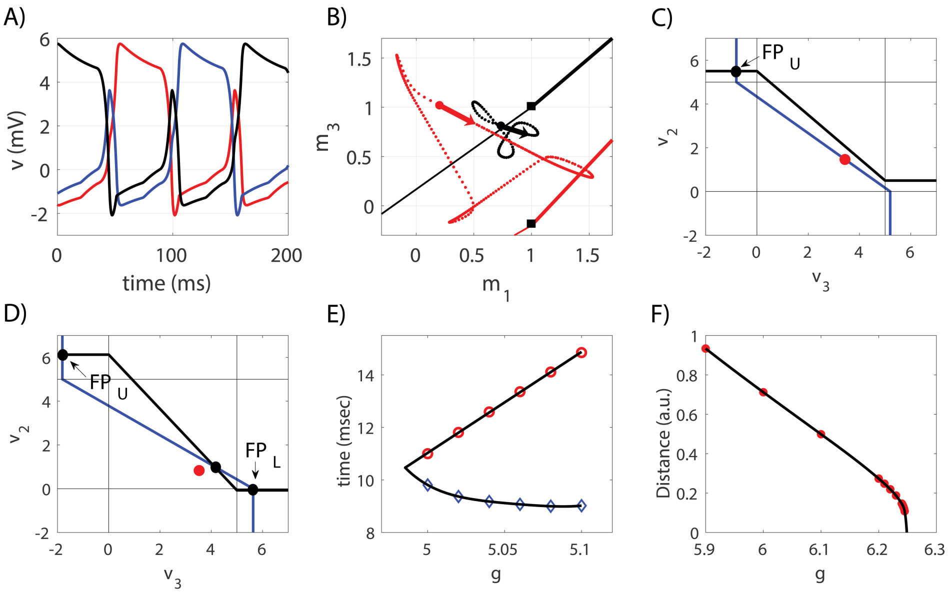

Figure 18. *UROs in the three-cell linear model system* (3.7). (A) *URO time course when* $g = 6.0$. *Red trace denotes* v_1, *blue* v_2, *and black* v_3. (B) *Projection of transition surfaces (lines) and trajectory of the full system (dots) onto* (m_1, m_3) *space for* $g = 5.0$ *(black) and* $g = 6.0$ *(red). In each case, the thick line denotes* Σ_2 *and the thin line* Σ_3, *which meet at a black square. Bigger dots on the trajectories denote the moment when* v_1 *assumes its maximum, at the start of the* v_1 *active phase.* (C)–(D) *Projection of the full system trajectory when* v_1 *turns off for* $g = 5.0$ (C) *and* $g = 6.0$ (D). *In both cases, the projection of the trajectory falls within the basin of attraction of* FP_U. (E) *When* v_1 *turns off after its active period, we measured two times, one for the fast dynamics to reach* FP_U *in* (v_3, v_2)*-space (blue diamonds) and the other for the loss of this fixed point (red circles) for* g *from* 5.0 *to* 5.1 *with stepsize* 0.02. *First- and fourth-order polynomials, respectively, were used to fit these curves. As* g *decreases toward* g_{pd3}, *the two curves approach and meet, such that UROs are lost.* (F) *When* v_1 *turns off after its active period, the distance between the projection of the trajectory of the full system and an approximation to the separatrix (the identity line in* (v_3, v_2)*-space) is measured for* g *from* 5.6 *to* 6.2 *with stepsize* 0.1, *from* 6.21 *to* 6.24 *with stepsize* 0.01, *and from* 6.241 *to* 6.245 *with stepsize* 0.001 *(red dots). Cubic splines are used for curve fitting. Positive distances correspond to positions in the basin of attraction of* FP_U. *As* g *approaches* g_{pd4}, *the distance decreases and finally vanishes, hence for* $g > g_{pd4}$, *we lose UROs.*

Copyright © by SIAM. Unauthorized reproduction of this article is prohibited.

Downloaded 09/04/22 to 130.49.198.139 . Redistribution subject to SIAM license or copyright; see https://epubs.siam.org/terms-privacy

the projection of the transition surfaces, Σ_2 and Σ_3 (solid line segments), onto (m_1, m_3)-space along with the projection of the trajectories of the full system (dotted curves) for $g = 5.0$ and $g = 6.0$ (refer to Figure 14 for comparison with DROs). The transition surfaces and full system trajectory for $g = 5.0$ and $g = 6.0$ are shown in black and red, respectively. As in DROs, the thick line denotes Σ_2 (equation (3.21)) and the thin line Σ_3 (equation (3.22)). The trajectories move downward and to the right since m_1 increases and m_3 decreases over the active period of v_1. As in DROs, the projected trajectories reach Σ_3 (adaptive escape) for smaller g and Σ_2 (adaptive release) for larger g. For example, when $g = 5.0$, the trajectory hits Σ_3 and when $g = 6.0$, the trajectory crosses Σ_2. Thus, we can conclude that UROs share with DROs the same mechanisms for the initiation of transition; that is, for small g, a transition is initiated by the increase of the voltage of one of the inhibited neurons through 0, which turns on its output, followed by the decrease of the voltage of the active neuron through v_{max}, whereas for large g, a transition results from the decrease of the active neuron's voltage through $v_{\max}$, which reduces its output, followed by the increase of the voltage of one of the inhibited neurons through 0.

Now we consider the interesting dynamics that arises during fast jumps within UROs, in which a previously silent neuron that appears to be on track to activate undergoes an abrupt switch from increasing to decreasing v and the other suppressed neuron activates next instead (Figure 18(A)). To investigate how this turn-around happens during transitions, we dissect the details of each step in the transition process. Again, we use the v_1-on state as an example for illustration. Once the transition is initiated through a saddle-node bifurcation that annihilates FP_L in (v_1, v_3)-space, the control of the system behavior switches from the (v_1, v_3) fast subsystem to the (v_3, v_2) fast subsystem. We will observe a transient in which v_3 initially increases above v_2 yet neuron 3 fails to activate if one of two conditions occurs. In the first scenario, FP_L in $(v_3,\ v_2)$-space is lost before the trajectory reaches it. For example, Figure 18(C) shows the projection of the trajectory (red dot) onto (v_3, v_2)-space along with the v_3-nullcline (blue) and the v_2-nullcline (black). We see that FP_L is not present, so the trajectory is forced to approach FP_U. In the second scenario, when v_1 turns off, the projection of the trajectory falls within the basin of attraction of FP_U (the region to the left of the separatrix), and hence although v_3 may increase as the trajectory initially travels close to the separatrix, the passage to FP_L is blocked; Figure 18(D) shows an example of this case.

Next, we discuss the loss of UROs at $g = g_{pd3}$ as g decreases and at $g = g_{pd4}$ as g increases (Figure 12). First, we find that the mechanism underlying the loss of UROs at $g = g_{pd3}$ is similar to that in DROs at $g = g_{pd2}$: the competition between the two times, one for the fast dynamics to equilibrate at the presumed fixed point (T_a) and the other for the bifurcation that annihilates that point (T_b). Figure 18(E) shows the plot of these two times under variation of parameter g (cf. Figure 17(F) for DROs). For $g < g_{pd3}$, UROs are lost and the trajectory of the full system approaches stable SOs (see Figure 12). On the other hand, the loss of UROs at $g = g_{pd4}$ is due to the position of the trajectory relative to the separatrix in the (v_3, v_2)-plane when v_1 turns off. Figure 18(F) shows that as g approaches g_{pd4}, the distance between the trajectories of the UROs and the separatrix decreases and finally becomes zero, corresponding to an exit from the basin of attraction of FP_U in the (v_3, v_2)-plane.

Copyright © by SIAM. Unauthorized reproduction of this article is prohibited.

Downloaded 09/04/22 to 130.49.198.139 . Redistribution subject to SIAM license or copyright; see https://epubs.siam.org/terms-privacy

3.2.5. What determines UROs and DROs?

The analysis that we have done helps to clarify whether DROs or UROs occur from any given set of initial conditions for parameter values for which the two solution types are bistable. For clarity, we continue to focus on the transition away from the v_1-on state. Recall that if m_1 is chosen at the fast subsystem bifurcation that terminates the v_1-on state, then the values of m_3, v_1, and v_3 are determined by (3.23) or (3.24). Moreover, we have assumed that we can perform a fast-slow decomposition, so we assume that the trajectory lies on the v_2-nullcline, with $v_2 = I - m_2 - gf(v_3) - g \cdot g_r$ in the adaptive escape case ($m_1 < I - v_{max}$) and $v_2 = I - m_2 - g \cdot g_r f(v_1)$ in the adaptive release case ($m_1 > I - v_{max}$). Hence, we can constrain our consideration of initial conditions to the plane of values of the remaining free variables, m_1 and m_2.

Numerical simulations of solution behavior were performed with (m_1, m_2) varied over a grid of values across successive simulations. For each run, we discarded an initial transient period and then checked the order of cell activations in the resulting trajectories to determine the solution type. These experiments show that two positively sloped curves, with positions that depend on g, partition the (m_1, m_2) plane into three regions: a lower right region that leads to UROs, with v_1 activation followed by v_2 and then v_3; a middle region that leads to DROs, with v_1 activation followed by v_3 and then v_2, which expands as g increases; and an upper left region that leads to a transient in which v_1 activation is followed by v_3 activation, then a second v_1 activation, and finally v_2 activation that transitions into sustained UROs. For visualization, we draw black solid boundary curves between these regions, such that all numerical experiments on opposite sides of the curve yielded distinct solution behaviors (Figures 19(A)–(C); however, note that the lower black curve is almost obscured by a green curve, which is discussed below).

We have also found that the boundary between DROs and UROs is closely related to the competition between two times, one for the trajectory of the full system to approach FP_L (T_a) and the other for the loss of FP_L to happen (T_b), during the transition in the (v_3, v_2)-plane. For (m_1, m_2) values away from the boundary in the DROs region, T_b is larger than T_a and thus the trajectory is able to approach FP_L in the (v_3, v_2)-plane. For (m_1, m_2) values near the boundary, however, these two times become comparable to each other. For (m_1, m_2) values in DROs near the boundary, T_a is slightly greater than T_b. For (m_1, m_2) values in UROs near the boundary, the trajectory fails to reach FP_L. More specifically, the unstable fixed point moves toward FP_L while the trajectory approaches FP_L, and the trajectory ends up in the basin for FP_U. As a result, the trajectory turns around and heads toward FP_U. The green curves in Figures 19(A), (B), and (C) are numerically computed curves where T_a and T_b are almost equal, and these lie quite close to the black dotted boundary curve between the DRO and URO regions obtained based on direct simulation of solution behavior as mentioned above.

We did one more numerical experiment to test our idea that the selection between DROs and UROs is determined by the values of m_1 and m_2 at the fast subsystem bifurcation that terminates the v_1-on state. In this experiment, we constructed a two-dimensional map from each subregion of (m_1, m_2) and checked if solution trajectories return to the same subregion after the transition between states takes place. For the lower UROs region, since the v_2-on state follows the v_1-on state, we checked the values of m_2 and m_3 at the fast subsystem bifurcation in the subsequent v_2-on state, such that (m_1, m_2) at the end of the v_1-on state is mapped to (m_2, m_3) at the end of the v_2-on state. For the middle DROs region, since the

Copyright © by SIAM. Unauthorized reproduction of this article is prohibited.

Downloaded 09/04/22 to 130.49.198.139 . Redistribution subject to SIAM license or copyright; see https://epubs.siam.org/terms-privacy

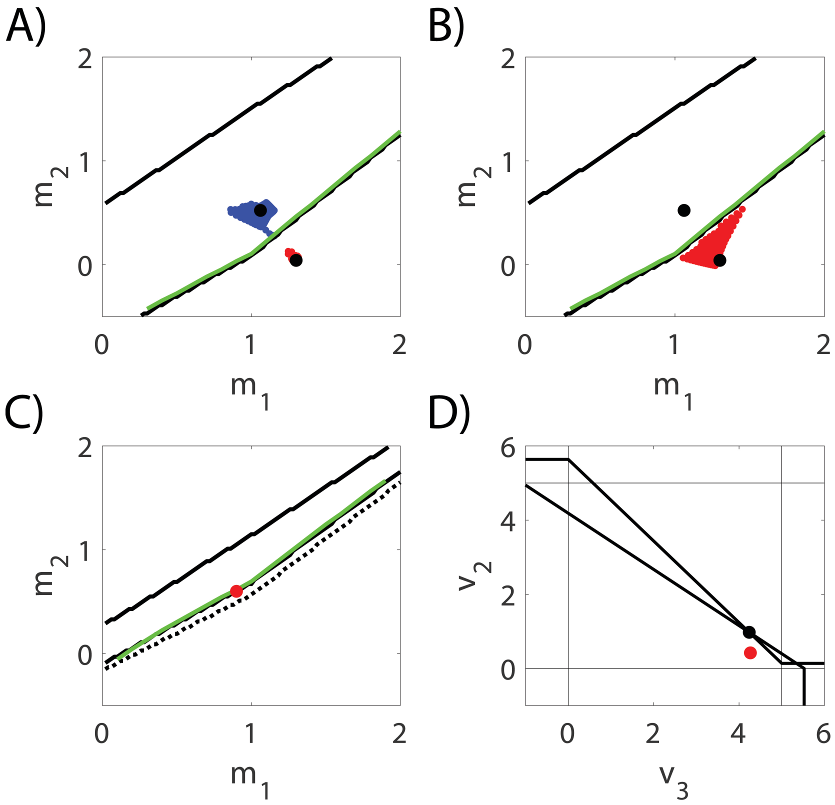

Figure 19. *Numerical exploration of attracting dynamics.* (A)–(B) *Images of two-dimensional maps based on dynamics of the adaptation variables when* $g = 5.8$. *An upper black curve separates an upper region where transient DROs are followed by UROs from a middle region where DROs occur. A lower black curve, almost covered by a green curve, separates the DRO region from a lower URO region (see text for more details). In* (A), *red (blue) dots indicate the image of a collection of points from the lower URO region (the middle DRO region). In* (B), *red dots indicate the image of a collection of points from the upper URO region. Black dots indicate the projections of the attracting URO and DRO solutions at the moment when* v_1 *turns off.* (C) *When* $g = 5.5$, *the lower URO region is divided by a dotted black curve into two subregions. In the upper (lower) subregion, when* v_1 *turns off, the projection lies in the region to the right (left) of the location of the separatrix—approximated locally by a line of slope* 1*—of the unstable fixed point of the fast dynamics shown in* (D). *For* $m_1 = 0.9$ *and* $m_2 = 0.6$ *(red dot in* (C)*), the projection of the trajectory when* v_1 *turns off is shown as the red dot in* (D). *The unstable fixed point in* (D) *is denoted by a black dot. As g increases, the black dotted curve approaches the black solid curve until the upper subregion disappears.*

v_3-on state follows the v_1-on state, we checked the values of m_3 and m_1 at the fast subsystem bifurcation in the v_3-on state, such that (m_1, m_2) at the end of the v_1-on state is mapped to (m_3, m_1) at the end of the v_3-on state. For the upper UROs region, since the v_3-on state first follows the v_1-on state, we also checked the values of m_3 and m_1 at the fast subsystem bifurcation in the subsequent v_3-on state, such that (m_1, m_2) at the end of the v_1-on state is again mapped to (m_3, m_1) at the end of the v_3-on state. In each subregion, we chose grid points with a stepsize of 0.1 in both the m_1 and m_2 directions and checked the images under the two-dimensional map. With an abuse of notation, all of the images of the grid points were plotted in $(m_1,\ m_2)$-space and the results are shown in Figures 19(A)–(B). The red dots in

Downloaded 09/04/22 to 130.49.198.139 . Redistribution subject to SIAM license or copyright; see https://epubs.siam.org/terms-privacy

Figure 19(A) show the images of the points from the lower URO region and the blue dots show the images of the points from the middle DRO region. We see that the two-dimensional map from the lower URO region is a contraction map, hence the solution trajectory stays in the lower URO region once it falls within that region, and similarly the map from the DRO region contracts to a smaller set within that region. The red dots in Figure 19(B) represent the images of the points from the upper URO region, which are all mapped into the lower URO region under the two-dimensional map (Figure 19(B)). This phenomenon can be explained heuristically as follows. For points in the upper URO region, we have $m_3 < m_1 \ll m_2$. After the fast bifurcation in the v_1-on state, m_1 decreases and m_3 increases. But, when v_1 turns off, m_3 is still sufficiently less than m_2 that v_3 succeeds to activate. In the subsequent v_3-on state, when the fast bifurcation happens, $m_1 \ll m_2$, and hence v_1 fires again, without v_2 firing in-between. As explained in Figure 19(A), once the trajectory falls within the lower URO region, it cannot escape, and hence UROs ensue.

Finally, Figure 19(C) shows for a slightly different g value that there is a band of (m_1, m_2) values near the boundary curve between the DRO region and the lower URO region where the slow dynamics plays an important role in selecting between UROs and DROs and turn-around of trajectories occurs. This region lies between the boundary curve (where the green and lower black curves coincide) and another curve shown in dotted black, and we chose a sample point in this region for purposes of illustration (red dot in Figure 19(C)). Using this point as our initial condition, we obtain UROs in which v_2 turns on after v_1, but if we consider the fast subsystem after v_1 turns off (Figure 19(D)), then we find that the projection of the trajectory (red dot in Figure 19(D)) lies in the region to the right of the separatrix associated with the unstable fixed point, which appears to be in the basin of the fixed point (FP_L) with v_3 on. However, similarly to what was demonstrated in Figure 17, through the slow dynamics, the fast subsystem fixed point FP_L is lost before v_3 fully activates and the trajectory subsequently approaches FP_U, with v_2 on, resulting in UROs. As g increases, this region where timescale mixing occurs becomes smaller and eventually disappears.

3.3. Full model revisited.

We now return to the full model, system (2.1) with $i = 1, 2, 3$ together with (2.2), (2.3), to apply the lessons learned from our analysis of simplified models. Our analysis shows that to explore the outcomes of transitions between phases, we should focus on the intersections of the nullsurfaces of the fast variables v_i in the three-dimensional fast subspace. For example, the nullsurface of v_1, say, N_1, is given by

$$v_1 = \frac{c_{u1} + a_{u1} f(v_2) + b_{u1} f(v_3)}{c_{l1} + a_{l1} f(v_2) + b_{l1} f(v_3)}, \tag{3.27}$$

where

$$a_{u1} = g_{\mathrm{SynI}} b_{21} v_{\mathrm{SynI}}, \qquad a_{l1} = g_{\mathrm{SynI}} b_{21},$$

$$b_{u1} = g_{\mathrm{SynI}} b_{31} v_{\mathrm{SynI}}, \qquad b_{l1} = g_{\mathrm{SynI}} b_{31},$$

$$c_{u1} = g_{\mathrm{AD}} m_1 v_{\mathrm{K}} + g_{\mathrm{L}} v_{\mathrm{L}} + g_{\mathrm{SynE}} D_1 v_{\mathrm{SynE}}, \qquad c_{l1} = g_{\mathrm{AD}} m_1 + g_{\mathrm{L}} + g_{\mathrm{SynE}} D_1.$$

We emphasize that all c_{ui} and c_{li}, and hence v_i, depend on m_i, and hence the shapes and positions of these nullsurfaces change as the slow variables m_i evolve.

Copyright © by SIAM. Unauthorized reproduction of this article is prohibited.

Downloaded 09/04/22 to 130.49.198.139 . Redistribution subject to SIAM license or copyright; see https://epubs.siam.org/terms-privacy

Figure 20 illustrates the transition from the v_2-on state to the v_3-on state during the URO shown in Figure 1(F), where v_1 initially rises but then falls back down again and makes way for v_3 activation. In this figure, the intersection of N_1 and N_2, say, C_{12}, is shown in blue and the intersection of N_2 and N_3, say, C_{23}, is shown in red. The black dots denote the intersection points of C_{12} and C_{23}, which are fixed points of the fast subsystem. The green dot is the projection of the trajectory of the whole system, which lies on top of and obscures a black dot in panels (A), (B), and (F). Black dotted curves are v_1- and v_2-nullclines projected onto the plane $v_3 = -70$ in (A)–(C), v_1- and v_3-nullclines projected onto the plane $v_2 = -70$ in (D)–(E), and v_3- and v_2-nullclines projected onto the plane $v_1 = -70$ in (F). The gray dot in each case is the projection of the trajectory of the whole system. Figure 20 illustrates that the transition from the v_2-on state to the v_3-on state is initiated by a change in the relationship between N_1 and N_2 (i.e., the geometry of C_{12}), which is induced by the slow dynamics that is not explicitly visible in this diagram. As time progresses and the slow variables evolve, two branches of C_{12} come together, merge, and finally disappear. In the process, two fixed points of the full system are lost in a saddle-node bifurcation, including the stable fixed point where the trajectory of the whole system resides. While the two branches of C_{12} grow closer (panels (A)–(B)), two new fixed points are created through the intersection of C_{12} and C_{23} toward the lower left corner of the plot. After the upper two fixed points merge and disappear, the trajectory of the whole system approaches one of the newly generated fixed points in the lower left region, which is stable (panel (C)). Switching to the (v_1, v_3)-projection in Figure 20(D), however, we see that the trajectory is blocked from reaching the fixed point associated with the v_1-on state due to the presence of an intervening saddle point. Instead, the trajectory lies in the basin of attraction of the stable v_3-on fixed point, to which it converges in Figures 20(E)–(F). After the trajectory of the whole system settles down on the lower right fixed point, the evolution of the slow variables causes the two previously lost fixed points to reappear. Similarly, the transition from v_3-on state to v_1-on state begins with the coalescence of the two branches of C_{23}.

Similar numerics reveals an analogous process in the DRO case, except without the turn-around component that arises in UROs such as in the transition from Figure 20(C) to Figure 20(D). For our parameter set, it appears that the loss of DROs with decreasing g in the full model occurs because the trajectory ends up on the other side of the separatrix and thus heads toward a different fixed point than for larger g, analogously to what we illustrate for UROs in the three-cell linear model in Figure 18(F), but we do not have a way to systematically analyze this transition in the full model.

Our linear analysis also highlights the utility of considering projections to two-dimensional slow or fast subspaces, corresponding to the variables involved in a transition. As part of this step, we can compute transition surfaces given by bifurcation curves. As we saw in the two-cell model for small g, we find that in our full model, only the transition surfaces for adaptive release, and not those for adaptive escape, arise in the relevant range of slow variables. Specifically, in the adaptive escape mechanism, the voltage of the active neuron needs to be higher than $v_{\max}$. But in the full model, the lower bound on m prevents the voltage of the active neuron from reaching this value. Figure 21(A) ((C), resp.) shows the transition surface Σ_2 (black curve) with the projection of the trajectory (red dots) for UROs (DROs, resp.) when $g_{\text{SynI}} = 70$. As in our previous figures, the large dot on the projection

Copyright © by SIAM. Unauthorized reproduction of this article is prohibited.

Downloaded 09/04/22 to 130.49.198.139 . Redistribution subject to SIAM license or copyright; see https://epubs.siam.org/terms-privacy

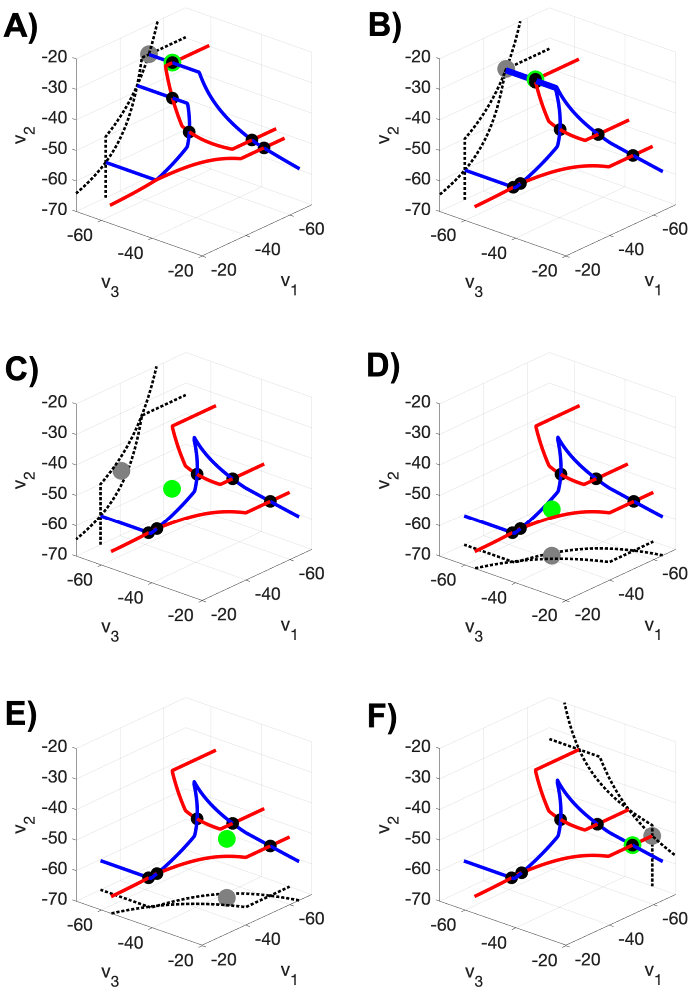

Figure 20. *Transition from the v_2-on state to the v_3-on state shown in Figure 1(F) for the original model (2.1). Blue (red, resp.) curves, C_{12} (C_{23}, resp.), are the intersections of the v_1- and v_2-nullsurfaces (v_2- and v_3-, resp.). Black dots, the intersection points of C_{12} and C_{23}, are fixed points of the fast subsystem. The green dot is the projection of the trajectory of the whole system. Black dotted curves are v_1- and v_2-nullclines projected onto the plane $v_3 = -70$ in* (A)–(C), *v_1- and v_3-nullclines projected onto the plane $v_2 = -70$ in* (D)–(E), *and v_3- and v_2-nullclines projected onto the plane $v_1 = -70$ in* (F). *Gray dot is the projection of the trajectory of the whole system.* (A) *The trajectory rests at the upper stable fixed point of the fast subsystem, where v_2 is on.* (B) *As time increases, two branches of C_{12} coalesce and the upper stable fixed point is lost.* (C) *As the transition progresses, the trajectory starts toward a fixed point on the lower left part of the diagram where v_1 would be on and v_2, v_3 would be off.* (D)–(E) *When the output from v_2 turns off, however, we see in the projection to the (v_1, v_3) plane, the path to the fixed point with v_1 on is blocked. Correspondingly, the trajectory turns around and approaches a different fixed point on the lower right part of the diagram.* (F) *Along this approach, v_1 turns off and the trajectory converges to the lower right fixed point, where v_3 is on. From* (A) *to* (F), *$t = 0, 390, 448, 450, 452, 480$ ms (bifurcation parameter $s = 0, 0.26, 0.2987, 0.3, 0.3013, 0.32$).*

Copyright © by SIAM. Unauthorized reproduction of this article is prohibited.

Downloaded 09/04/22 to 130.49.198.139 . Redistribution subject to SIAM license or copyright; see https://epubs.siam.org/terms-privacy

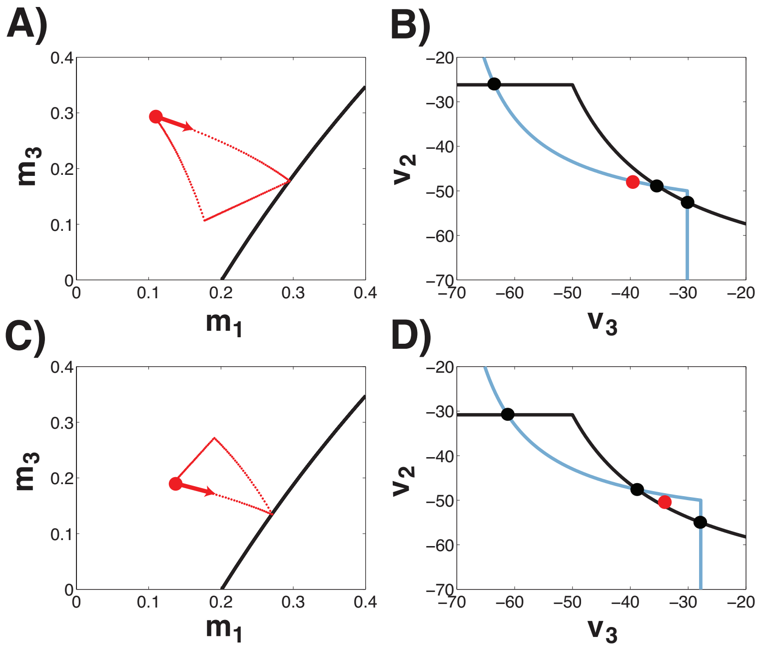

Figure 21. *Example projections of solutions from the full model* (2.1)*. First row shows UROs when* $g = 70$ *and second row DROs when* $g = 70$*. Figures in left column show* Σ_2 *(black) and projection of trajectory of slow system system (dots) onto* (m_1, m_3) *space. As before, bigger dots on the projection of each trajectories denote the moment when* v_1 *assumes its maximum. In UROs, the projection of trajectory rotates clockwise and in DROs, counterclockwise. Figures in right column show nullclines of fast variables when* v_1 *turns off. In each case,* v_3 *nullcline (black) and* v_2 *nullcline (blue) intersect at three points. In UROs, the projection of trajectory of the full system (red dot) falls within the region left to the separatrix and in DROs, within the region right to the separatrix.*

of the trajectory indicates the moment when v_1 assumes its maximum over its active period. Over the active period of v_1, m_1 increases and m_3 decreases, hence the projection of the trajectory moves downward to the right and finally hits Σ_2 to initiate the transition away from the v_1-on state. In UROs, the projection of the trajectory evolves clockwise, and in DROs, counterclockwise. As in the linear model, the structure of the fast subsystem during the fast jumps, which depends on the values of slow variables at the fast subsystem bifurcation and during the transition, determines the transition outcomes. Figure 21(B) ((D), resp.) shows the projection of the trajectory (red dot) in (v_3, v_2)-space in UROs (DROs, resp.) when $g_{\text{SynI}} = 70$, along with the v_3- and v_2-nullclines (blue). As in linear model, in the URO case, the projected trajectory lies in the basin of attraction of FP_U in (v_3, v_2)-space (Figure 21(B)), while in the DRO case, the projection of the trajectory falls within the basin of attraction of FP_L in (v_3, v_2)-space (Figure 21(D)). Note, however, that simply being in the basin of attraction of a fixed point does not guarantee that a trajectory will approach that fixed point monotonically; as seen in Figure 20, in the full three-dimensional fast flow, the trajectory's path may be complicated and may appear to go toward the separatrix in certain directions before it moves away.

Copyright © by SIAM. Unauthorized reproduction of this article is prohibited.

Downloaded 09/04/22 to 130.49.198.139 . Redistribution subject to SIAM license or copyright; see https://epubs.siam.org/terms-privacy

4. Discussion.

In this study, we analyzed activity patterns of a three-unit neuronal network with all-to-all inhibitory synaptic coupling. Such inhibitory circuits often arise as building blocks of CPG models because of the prevalence of inhibitory interneurons within these networks and because mutual inhibition provides a natural framework for producing the sequential activation patterns seen in muscle groups driven by CPG outputs. The main contributions of this work include a bifurcation study that reveals the existence of a large parameter range over which bistability in oscillation patterns occurs, a mathematical analysis of the mechanisms involved in generating these patterns, and an explanation of the role of fast and slow timescale interaction in shaping phase transitions in this model. The use of linear models allowed us to proceed with the mathematical analysis that we performed, which was critical for obtaining a variety of mechanistic insights and for providing evidence that the effects revealed by our numerical simulations are valid. Although we did not derive the linear model rigorously from the nonlinear one, we provide a rationale for its form, and numerical experiments (e.g., Figures 2(C), (D) versus Figure 12; Figure 20; and Figures 17, 18 versus Figure 21) suggest that the results obtained hold qualitatively for the full, nonlinear system (2.1)–(2.3), with the nonlinearities in adaptation and inhibition in the full model affecting quantitative aspects of system behavior and determining which specific mechanisms arise for specific parameter sets.

CPG circuits represent a natural subject for computational and mathematical study in part because some, such as the crustacean stomatogastric ganglion, are experimentally accessible, allowing for the extraction of information to inform models and the testing of theoretical predictions; moreover, mechanistic principles that are derived from modeling work and simplified settings provide a starting point for attempts to understand other CPGs, such as those that drive mammalian locomotion, which are much more complex and less accessible. Correspondingly, there has been extensive work on this topic in the literature, but plenty of questions about CPGs have not yet been addressed.

We have identified six lessons from this study that we feel are the most interesting takeaways. First, our work identifies and analyzes robust bistability between smooth oscillations and relaxation-type oscillations as well as between two classes of relaxation oscillations featuring different activation orders (Figures 1, 2, 12), despite a coupling anisotropy that would appear to favor a unique direction of propagation. Previous work on simple three-unit neuron models with inhibition has also highlighted bi- and multistability. For some CPG functions, such as respiration, changes in activation order could be problematic. Interestingly, although evidence suggests that the core respiratory CPG includes a three-cell inhibitory ring [29], at least one of the nodes in the ring also includes an excitatory neuron population, and this additional component may help to enforce a functional activation order. In other CPGs, bi- or multistability seems like a desirable feature, to allow intentional modulation of outputs, such as switches between forward and backward stepping or between swimming and scratching or stepping movements. In the latter context, this work supports the argument in the literature [2, 5] that the same CPG circuit can be used to generate diverse motor outputs. A series of earlier computational papers starting with work by Wojcik, Clewley, and Shilnikov [50] has extensively documented the output patterns of three-neuron inhibitory circuit models and their dependence on a range of parameters, including some bifurcation studies [8]. These works use fast threshold modulation [46], in which coupling strength instantaneously jumps when voltage crosses a threshold, in contrast to the continuously-voltage-dependent coupling

Copyright © by SIAM. Unauthorized reproduction of this article is prohibited.

Downloaded 09/04/22 to 130.49.198.139 . Redistribution subject to SIAM license or copyright; see https://epubs.siam.org/terms-privacy

that we consider. Moreover, these studies are numerical, whereas our work illustrates the dynamic mechanisms that determine network activity patterns. Another analytical study on this topic also focused on a rich variety of possible activation orders within these circuits, including alternatives to 1,2,3,... and 1,3,2,... in which individual units may activate more than once per period (e.g., 1,2,1,3,1,2,...) [39]. That study, however, also had instantaneous turn-on and turn-off of inhibition and did not consider multistability.

A second lesson of our work is that adaptation together with inhibition can give nonintuitive effects. Indeed, these effects provide part of the explanation of how we can obtain robust bistability despite a bias in the coupling strength that would seem to favor a specific activation order. Stronger inhibition can be paradoxically advantageous to a neuron's subsequent activation because it can help adaptation to wear off faster, achieving a lower level while a neuron is suppressed by another cell's activity. A similar effect is known in settings in which inhibitory inputs are required to allow a neuron to fire, such as post-inhibitory rebound [49] or postinhibitory facilitation [11, 36]. Indeed, a somewhat similar principle could allow a sufficiently strongly inhibited neuron to fire in response to removal of inhibition, whereas a more weakly inhibited neuron would not.

A third lesson of our work returns to the issue of the form of the coupling function that we consider. The use of synaptic coupling that jumps instantaneously between on and off states is popular in theoretical and computational studies because it simplifies analysis and it reduces the number of parameters to be tuned compared to other alternatives. Following previous work [35], we use a coupling function that linearly grows with voltage between lower and upper bounds. As a result, when a neuron's activation ends and its inhibition of its suppressed partners thus terminates, both of the other neurons' voltages can rise above the lower bound, allowing them to exert partial inhibition on each other as they compete to reach the upper voltage bound, which we take as our representation of activation. In particular, a participant in this competition that had been more strongly inhibited by the previously active neuron will now more strongly inhibit its competitor than vice versa. Although the competitor may start with a higher voltage, this disparity in inhibition contributes to the apparent switching that we observe (e.g., Figures 1(F), 3, 12(D)), in which one neuron's voltage overtakes another's during phase transitions in UROs. The idea of synaptic release kicking in from a relatively low voltage may initially seem strange. But here, we use nonspiking neural units, which can be thought of as representing the average state of a population that is synchronized in terms of its activation state but not its spiking. When an average voltage is low but above rest in this model, this would correspond to a low but nonzero spiking rate in a population, with a corresponding low but nonzero level of synaptic release.

Fourth, and still related to the coupling in the model, we find phase transitions that occur through effects that we term *adaptive escape* and *adaptive release* (Figures 13–16). These effects are generalizations of classical escape and release [48, 43] as well as synaptic escape and release [42] that involve a gradual change in coupling level (see also [9, 35]). In adaptive escape and release, one neuron's voltage crosses into the regime of linear synaptic dependence on voltage, but this event does not allow an immediate phase transition. Rather, a change in the neurons' activation status requires a second neuron to cross into this regime. Nonetheless, this second crossing is only possible because the first one occurred. Hence, adaptive escape and release are cooperative events in which two neurons together engineer a transition. This

Copyright © by SIAM. Unauthorized reproduction of this article is prohibited.

Downloaded 09/04/22 to 130.49.198.139 . Redistribution subject to SIAM license or copyright; see https://epubs.siam.org/terms-privacy

mechanism does not strictly require continuous coupling: in theory, if an active cell crossed an all-or-none synaptic threshold while still staying active, that crossing could destabilize a resting state critical point of a suppressed neuron yet, due to the configuration of its voltage nullcline, the silent neuron could still need to evolve for some time in phase space before escaping from the silent phase and hence initiating a phase transition. Nonetheless, adaptive escape and release become natural and robust to parameter variations with continuous coupling, although classic escape and release may also occur.

The issue of nullcline configurations brings us to a fifth lesson, related to mixing of timescales. Because CPG networks' outputs exhibit extended phases with one neuron or population active, followed by rapid activation switches, and because CPG neurons tend to feature voltage-dependent currents with slowly varying aspects (e.g., slow inactivation of persistent sodium current or dependence of certain currents on slowly varying calcium levels), CPG models often can be considered using ideas of fast-slow decomposition (cf. [34, 9, 35]). In fast-slow decomposition for a two-dimensional neural oscillator, the voltage is the fast variable and some other variable, such as an adaptation level, is slow. Trajectories rapidly converge to a small neighborhood of an attracting branch of the voltage nullcline, after which they slowly evolve along that branch under the dynamics of the slow variable. When a trajectory reaches a fold of the nullcline where the branch ends, corresponding to a saddle-node bifurcation of the fast equation with the slow variable treated as a parameter, the fast dynamics takes control again, a fast switch in neural activation occurs, and then another slow regime follows. In the reduced models that we study, because of the form of the coupling, the fast nullcline branches or surfaces can lie close together, allowing a mixing of timescales. Specifically, as a trajectory approaches a stable critical point of the fast dynamics, the slow variables can change enough to induce a bifurcation in the fast subsystem that annihilates that critical point, causing the fast dynamics to change course (Figures 17, 19(C)–(D)). An analysis that completely separates fast jumps between fast subsystem attractors alternating with slow passages along these attractors would produce incorrect results. In the full model, we expect that similar effects are occurring, combined with more complicated dynamics in the fast subsystem itself.

The above discussion focuses on the critical points of the fast dynamics. In our analysis of the slow dynamics of our reduced models, however, a sixth lesson emerged. Within each phase of a rhythm, the slow dynamics features an attracting critical point. From the relevant regions of the slow phase space, however, trajectories converging to such a critical point would cross a threshold at which a bifurcation of the fast subsystem would be induced (e.g., fixed points of slow dynamics lie outside the kite illustrated in Figure 9, across the Σ_i curves that bound it). Thus, with respect to the slow timescale, the vector field could suddenly change, and the location of the slow subsystem attractor would move as part of that transition. In other words, the critical points were effectively illusory. Thus, this work illustrated the point, seen previously in other contexts [17, 12, 23], that in systems with switching, critical points that are outside of the relevant phase space domain can still be influential. This point will be explored further in the neural circuit setting in future work.

In this study, piecewise-smoothness of the coupling function allows us to dissect the fast dynamics in a piecewise way and we found that there are three possible scenarios that may arise during phase transitions, which relate to the interplay between the fast dynamics and slow dynamics. We found that the fast subspace during transitions is locally divided into three

Copyright © by SIAM. Unauthorized reproduction of this article is prohibited.

Downloaded 09/04/22 to 130.49.198.139 . Redistribution subject to SIAM license or copyright; see https://epubs.siam.org/terms-privacy

subregions over which three different outcomes will emerge (cf. Figure 19). In one region, the fast dynamics equilibrates in a standard way to a fixed point manifold; this outcome happens in stabilized DROs. In another region, the fixed point manifold that would be expected to attract the fast dynamics either is not present or is inaccessible due to a separatrix of the fast subsystem, and the fast dynamics approaches another manifold of stable fixed points. This outcome happens in stabilized UROs (e.g., Figures 20, 21). The most interesting case is when the fast dynamics falls within the region between these two regimes. In this region, the fast dynamics tries to settle down on a fixed point manifold but the slow dynamics pushes the fast subsystem through a bifurcation, hence the fixed point manifold that appears to be the target of the fast dynamics disappears and the fast subsystem trajectory is forced to approach a new fixed point manifold directly (Figure 17(D)). On the second and third regions, turn-around during fast jumps occurs. In general, trajectories enter the third region not within stabilized UROs or DROs but rather during transients, such as those that occur, for example, when the system behavior is far away from a stable periodic orbit due to a choice of initial condition. But, as the bifurcation parameter, g, approaches bifurcation points at which solution branches destabilize, we find an increase in the volume of initial conditions for which this possibility occurs. For example, as g approaches g_{pd2}, where the stable DRO branch terminates, from the right, the projection of the fast dynamics at the moment when an active neuron turns off approaches the boundary between the first and the third regions (Figure 17(E)). We found that the same mechanism applies when g approaches g_{pd3}, where UROs terminate, from the right (Figure 18(E)). On the other hand, when g approaches g_{pd4}, at the other end of the URO branch, from the left, the projection of the fast dynamics when an active neuron turns off approaches the boundary of the second region (Figure 18(F)).

Although this work gives rise to this variety of observations, plenty of open issues concerning small neural circuits remain, including questions about the capabilities of individual circuits to produce multiple rhythms, about the coordination of interacting CPG networks, and about the mechanisms such as neuromodulation and other feedback and drive signals that control and tune CPG outputs. Many of these questions will require moving beyond the three-cell motif, yet it is worth keeping in mind that small circuits provide a relatively tractable arena for the extraction of dynamic principles, which can provide useful predictions for larger models and for experiments.

REFERENCES

[1] B. J. Bacak, T. Kim, J. C. Smith, J. E. Rubin, and I. A. Rybak, *Mixed-mode oscillations and population bursting in the pre-Bötzinger complex*, eLife, 5 (2016), e13403.

[2] A. Berkowitz, *Both shared and specialized spinal circuitry for scratching and swimming in turtles*, J. Compar. Physiol. A, 188 (2002), pp. 225–234.

[3] R. Bertram and J. E. Rubin, *Multi-timescale systems and fast-slow analysis*, Math. Biosci., 287 (2017), pp. 105–121.

[4] B. Bondy, A. N. Klishko, D. H. Edwards, B. I. Prilutsky, and G. Cymbalyuk, *Control of cat walking and paw-shake by a multifunctional central pattern generator*, in Neuromechanical Modeling of Posture and Locomotion, Springer, New York, 2016, pp. 333–359.

[5] K. Briggman and W. Kristan, Jr., *Multifunctional pattern-generating circuits*, Annu. Rev. Neurosci., 31 (2008), pp. 271–294.

[6] G. Buzsaki, *Rhythms of the Brain*, Oxford University Press, Oxford, UK, 2006.

Copyright © by SIAM. Unauthorized reproduction of this article is prohibited.

[7] M. G. Codianni, S. Daun, and J. E. Rubin, *The roles of ascending sensory signals and top-down central control in the entrainment of a locomotor CPG*, Biol. Cybernet., 114 (2020), pp. 533–555.

[8] J. Collens, K. Pusuluri, A. Kelley, D. Knapper, T. Xing, S. Basodi, D. Alacam, and A. Shilnikov, *Dynamics and bifurcations in multistable* 3*-cell neural networks*, Chaos, 30 (2020), 072101.

[9] S. Daun, J. E. Rubin, and I. A. Rybak, *Control of oscillation periods and phase durations in half-center central pattern generators: A comparative mechanistic analysis*, J. Comput. Neurosci., 27 (2009), p. 3.

[10] S. Daun-Gruhn, *A mathematical modeling study of inter-segmental coordination during stick insect walking*, J. Comput. Neurosci., 30 (2011), pp. 255–278.

[11] R. Dodla, G. Svirskis, and J. Rinzel, *Well-timed, brief inhibition can promote spiking: Postinhibitory facilitation*, J. Neurophysiol., 95 (2006), pp. 2664–2677.

[12] R. Edwards, *Analysis of continuous-time switching networks*, Phys. D, 146 (2000), pp. 165–199.

[13] A. K. Engel, P. Fries, and W. Singer, *Dynamic predictions: Oscillations and synchrony in top-down processing*, Nat. Rev. Neurosci., 2 (2001), pp. 704–716.

[14] B. Ermentrout, *Simulating, Analyzing, and Animating Dynamical Systems: A Guide to XPPAUT for Researchers and Students*, SIAM, Philadelphia, 2002.

[15] W. O. Friesen, *Reciprocal inhibition: A mechanism underlying oscillatory animal movements*, Neuroscience Biobehavioral Reviews, 18 (1994), pp. 547–553.

[16] P. A. Getting, *Emerging principles governing the operation of neural networks*, Annu. Rev. Neurosci., 12 (1989), pp. 185–204.

[17] L. Glass and J. S. Pasternack, *Stable oscillations in mathematical models of biological control systems*, J. Math. Biol., 6 (1978), pp. 207–223.

[18] M. Golubitsky and I. Stewart, *Recent advances in symmetric and network dynamics*, Chaos, 25 (2015), 097612.

[19] M. Golubitsky, I. Stewart, P.-L. Buono, and J. Collins, *A modular network for legged locomotion*, Phys. D, 115 (1998), pp. 56–72.

[20] S. Grillner, *Biological pattern generation: The cellular and computational logic of networks in motion*, Neuron, 52 (2006), pp. 751–766.

[21] Z.-Z. Hao, L. E. Spardy, E. B. Nguyen, J. E. Rubin, and A. Berkowitz, *Strong interactions between spinal cord networks for locomotion and scratching*, J. Neurophysiol., 106 (2011), pp. 1766–1781.

[22] E. M. Izhikevich and R. FitzHugh, *Fitzhugh-Nagumo model*, Scholarpedia, 1 (2006), p. 1349.

[23] L. Lu and R. Edwards, *Structural principles for periodic orbits in glass networks*, J. Math. Biol., 60 (2010), pp. 513–541.

[24] E. Marder, *Motor pattern generation*, Curr. Opin. Neurobiol., 10 (2000), pp. 691–698.

[25] E. Marder and D. Bucher, *Central pattern generators and the control of rhythmic movements*, Current Biology, 11 (2001), pp. 986–996.

[26] E. Marder and R. Calabrese, *Principles of rhythmic motor pattern generation*, Physiol. Rev., 76 (1996), pp. 687–717.

[27] Y. I. Molkov, B. J. Bacak, T. E. Dick, and I. A. Rybak, *Control of breathing by interacting pontine and pulmonary feedback loops*, Front. Neural Circuits, 7 (2013), 16.

[28] Y. I. Molkov, B. J. Bacak, A. E. Talpalar, and I. A. Rybak, *Mechanisms of left-right coordination in mammalian locomotor pattern generation circuits: A mathematical modeling view*, PLoS Comput. Biol., 11 (2015), e1004270.

[29] Y. I. Molkov, J. E. Rubin, I. A. Rybak, and J. C. Smith, *Computational models of the neural control of breathing*, Wiley Interdiscip. Rev. Systems Biology Medicine, 9 (2017), e1371.

[30] C. Morris and H. Lecar, *Voltage oscillations in the barnacle giant muscle fiber*, Biophys. J., 35 (1981), pp. 193–213.

[31] J. Parker, B. Bondy, B. I. Prilutsky, and G. Cymbalyuk, *Control of transitions between locomotor-like and paw shake-like rhythms in a model of a multistable central pattern generator*, J. Neurophysiol., 120 (2018), pp. 1074–1089.

[32] J. Parker, R. Khwaja, and G. Cymbalyuk, *Asymmetric control of coexisting slow and fast rhythms in a multifunctional central pattern generator: A model study*, Neurophysiology, 51 (2019), pp. 390–399.

Downloaded 09/04/22 to 130.49.198.139 . Redistribution subject to SIAM license or copyright; see https://epubs.siam.org/terms-privacy

Copyright © by SIAM. Unauthorized reproduction of this article is prohibited.

[33] D. Richter and D. Ballantyne, *A three phase theory about the basic respiratory pattern generator*, in Central Neurone Environment and the Control Systems of Breathing and Circulation, Springer, New York, 1983, pp. 164–174.

[34] J. Rinzel, *A formal classification of bursting mechanisms in excitable systems*, in Proceedings of the International Congress of Mathematicians, A. Gleason, ed., AMS, Providence, RI, 1987, pp. 1578–1594.

[35] J. E. Rubin, N. A. Shevtsova, G. B. Ermentrout, J. C. Smith, and I. A. Rybak, *Multiple rhythmic states in a model of the respiratory central pattern generator*, J. Neurophysiol., 101 (2009), pp. 2146–2165.

[36] J. E. Rubin, J. Signerska-Rynkowska, and J. D. Touboul, *Type* III *responses to transient inputs in hybrid nonlinear neuron models*, SIAM J. Appl. Dyn. Syst., 20 (2021), pp. 953–980.

[37] J. E. Rubin and J. C. Smith, *Robustness of respiratory rhythm generation across dynamic regimes*, PLoS Comput. Biol., 15 (2019), e1006860.

[38] J. E. Rubin and D. Terman, *Geometric singular perturbation analysis of neuronal dynamics*, in Handbook of Dynamical Systems, vol. 2, Elsevier, Amsterdam, 2002, pp. 93–146.

[39] J. E. Rubin and D. Terman, *Explicit maps to predict activation order in multiphase rhythms of a coupled cell network*, J. Math. Neurosci., 2 (2012), pp. 1–28.

[40] I. A. Rybak, A. P. Abdala, S. N. Markin, J. F. Paton, and J. C. Smith, *Spatial organization and state-dependent mechanisms for respiratory rhythm and pattern generation*, Prog. Brain Res., 165 (2007), pp. 201–220.

[41] I. A. Rybak, N. A. Shevtsova, M. Lafreniere-Roula, and D. A. McCrea, *Modelling spinal circuitry involved in locomotor pattern generation: Insights from deletions during fictive locomotion*, J. Physiol., 577 (2006), pp. 617–639.

[42] M. Sekerli and R. J. Butera, *Oscillations in a simple neuromechanical system: Underlying mechanisms*, J. Comput. Neurosci., 19 (2005), pp. 181–197.

[43] F. K. Skinner, N. Kopell, and E. Marder, *Mechanisms for oscillation and frequency control in reciprocally inhibitory model neural networks*, J. Comput. Neurosci., 1 (1994), pp. 69–87.

[44] J. C. Smith, A. Abdala, H. Koizumi, I. A. Rybak, and J. F. Paton, *Spatial and functional architecture of the mammalian brain stem respiratory network: A hierarchy of three oscillatory mechanisms*, J. Neurophysiol., 98 (2007), pp. 3370–3387.

[45] A. C. Snyder and J. E. Rubin, *Conditions for multi-functionality in a rhythm generating network inspired by turtle scratching*, J. Math. Neurosci., 5 (2015), pp. 1–34.

[46] D. Somers and N. Kopell, *Rapid synchronization through fast threshold modulation*, Biolog. Cybern., 68 (1993), pp. 393–407.

[47] D. Terman, N. Kopell, and A. Bose, *Dynamics of two mutually coupled slow inhibitory neurons*, Phys. D, 117 (1998), pp. 241–275.

[48] X.-J. Wang and J. Rinzel, *Alternating and synchronous rhythms in reciprocally inhibitory model neurons*, Neural Comput., 4 (1992), pp. 84–97.

[49] X.-J. Wang and J. Rinzel, *Spindle rhythmicity in the reticularis thalami nucleus: Synchronization among mutually inhibitory neurons*, Neuroscience, 53 (1993), pp. 899–904.

[50] J. Wojcik, R. Clewley, and A. Shilnikov, *Order parameter for bursting polyrhythms in multifunctional central pattern generators*, Phys. Rev. E, 83 (2011), 056209.

[51] J. Wojcik, J. Schwabedal, R. Clewley, and A. L. Shilnikov, *Key bifurcations of bursting polyrhythms in* 3*-cell central pattern generators*, PloS One, 9 (2014), e92918.

[52] R. Yuste, J. MacLean, J. Smith, and A. Lasner, *The cortex as a central pattern generator*, Nature Rev. Neurosci., 6 (2005), pp. 477–483.

Downloaded 09/04/22 to 130.49.198.139 . Redistribution subject to SIAM license or copyright; see https://epubs.siam.org/terms-privacy

Copyright © by SIAM. Unauthorized reproduction of this article is prohibited.